Engineering with Computers (2021) 37:3489–3508
https://doi.org/10.1007/s00366-020-01004-z

ORIGINAL ARTICLE

The critical voltage of a GPL-reinforced composite microdisk covered with piezoelectric layer

Erfan Shamsaddini Lori[1] · Farzad Ebrahimi[2] · Eris Elianddy Bin Supeni[1] · Mostafa Habibi[3] · Hamed Safarpour[2]

Received: 8 October 2019 / Accepted: 6 March 2020 / Published online: 23 March 2020
© Springer-Verlag London Ltd., part of Springer Nature 2020

Abstract
In this research, electrically characteristics of a graphene nanoplatelet (GPL)-reinforced composite (GPLRC) microdisk are explored using generalized differential quadrature method. Also, the current microstructure is coupled with a piezoelectric actuator (PIAC). The extended form of Halpin–Tsai micromechanics is used to acquire the elasticity of the structure, whereas the variation of thermal expansion, Poisson's ratio, and density through the thickness direction is determined by the rule of mixtures. Hamilton's principle is implemented to establish governing equations and associated boundary conditions of the GPLRC microdisk joint with PIAC. The compatibility conditions are satisfied by taking perfect bonding between the core and PIAC into consideration. Maxwell's equation is employed to capture the piezoelectricity effects. The numerical results revealed the important role of ratios of length scale and nonlocal to thickness, outer-to-inner ratio of radius (R_o/R_i), ratio of piezoelectric to core thickness (h_p/h), and GPL weight fraction (g_{GPL}) on the critical voltage of the system. Another important consequence is that by increasing R_o/R_i, the critical voltage of the smart structure increases more intensely in comparison with the g_{GPL}.

Keywords Piezoelectric layer · GPLRC · Electrically characteristics · Microdisk · Compatibility equations · GDQM

1 Introduction

Reinforced laminated composites are increasingly used in various applications due to its outstanding features, namely high tensile strength, high modulus, and lightweight [1–20]. Because of some important requirements in science and technology for promoting the mechanical response and performance of the systems, reinforcing with GPL attracted the attention of numerous researchers for providing an impressive enhancement in the construction of the practical composite structures. Also, frequency response is more important in many applications [21–31]. Suna et al. [32] performed a study to compare the fracture performance of the functionally graded (FG) cemented carbide in the presence and absence of GPL reinforcement. They concluded that the superb properties of GPLs in the content of nanocomposites can be considered as a barrier in the way of growing microcracks. Also, according to the results of an experimental study, Rafiee et al. [33] asserted that the composites reinforced with GPL present more strength in comparison with the structures employing SWCNT, DWCNT, and MWCNT as the reinforcement. In the current decade, exploring the dynamic response of GPL-reinforced nanostructures becomes the hot topic of many surveys as a consequence of remarkable progress in nanotechnologies. In this field of research, the stability and the vibrational response of a thermo-elastic circular plate are analyzed in Refs [11–16, 34–59]. Vibration, buckling, wave propagation, and bending responses of the nanocomposite-reinforced structures are investigated in Refs. [60–65].

High-speed rotation and exposure to the thermal site are considered as the main assumptions in the mathematical modeling of the system to acquire the critical spinning speed

✉ Farzad Ebrahimi
febrahimy@gmail.com

✉ Eris Elianddy Bin Supeni
eris@upm.edu.my

1 Department of Mechanical and Manufacturing Engineering, Faculty of Engineering, Universiti Putra Malaysia, Seri Kembangan, Malaysia

2 Department of Mechanics, Faculty of Engineering, Imam Khomeini International University, Qazvin, Iran

3 Center of Excellence in Design, Robotics, and Automation, School of Mechanical Engineering, Sharif University of Technology, Tehran, Iran

of thermos-whirling circular plates. The impressive effect of damping coefficients on the transient forced oscillation and stability of the FG circular plate with viscoelastic boundary edges is revealed by Alipour [66]. Within the framework of classical theory, Ebrahimi and Rastgoo [67] explored solution methods to analyze the vibration performance of the FG circular plate covered with piezoelectric. As another survey, Ebrahimi and Rastgoo [68] studied flexural natural frequencies of FG annular plate coupled with layers made of piezoelectric materials. Shasha et al. [69] introduce a novel exact model on the basis of surface elasticity and Kirchhoff theory to determine the vibration performance of a double-layered microcircular plate. The surface effect is captured in their model as the main novelty. The results obtained with the aid of their modified model showed that the vibration performance of the double-layered microstructure is quite higher than the single-layered one. On the basis of FSD theory, Mohammadimehr et al. [70] conducted a numerical study in the dynamic and static stability performance of a composite circular plate by implementing GDQM. Moreover, they considered the thermo-magnet field to define the sandwich structure model. As another work, Mohammadimehr et al. [71] applied DQM in the framework of MCS to describe stress filed and scrutinize the dynamic stability of an FG boron nitride nanotubes-reinforced circular plate. They claimed that using reinforcement in a higher volume fraction promotes the strength and vibration response of the structure. Nonlinear oscillation and stability of microcircular plates subjected to electrical field actuation and mechanical force are studied by Sajadi et al. [72]. They concluded that pure mechanical load plays a more dominant role on the stability characteristics of the structure in comparison with electromechanical load. Also, they confirmed the positive impact of AC or DC voltage on the stability of the system in different cases of application. In order to determine the critical angular speed of spinning circular shell coupled with sensor at its end, Safarpour et al. [36] applied GDQM to analyze forced and free oscillatory responses of the structure on the base of thick shell theory. Through a theoretical approach, Wang et al. [73] obtained critical temperature and thermal load of a nanocircular shell. Safarpour et al. [44] introduced a numerical technique with high accuracy to study the static stability, forced and free vibration performance of a nanosized FG circular shell in exposure to thermal site. In addition, some researchers showed that some geometrical and physical parameters have important role on the stability or instability of the structures [36–39, 40–52, 54, 74–77]. Based on the NSG theory, the nonlocal effects on the dynamic and static responses of the micro/nanostructure are presented in Refs. [61, 78–85].

Wang et al. [86] reported the nonlinear dynamic performance of size-dependent circular plates with the piezoelectric actuator in the exposure of a thermal site with the aid of MCS incorporated with surface elasticity theory to consider the size effects. They highlighted the considerable effect of geometrical nonlinearity on the dynamic characteristics of the system. By employing FSDT, NSGT, DQM, and Hamilton's principle, Mahinzare et al. [87] presented a comprehensive parametric investigation in the size-dependent vibration performance of FG circular plate by considering the electro-elastic, thermal, and rotational effects. They showed the considerable impact of spinning velocity on the natural frequencies of nanosized systems. In another investigation, the same authors [88] studied the size-dependent vibration response of a spinning two-directional FG circular plate integrated with the PIAC on the basis of DQM, Hamilton's principle, and FSDT. The results confirmed the high dependency of the dynamic performance of the circular plate to spinning load and external applied voltage. In a huge number of researches [79, 89–96], the results of nonlocal elasticity compared with those results by nonlocal strain gradient elasticity.

None of the published articles focused on analyzing the electrically analysis of the GPLRC microdisk joint with PIAC using NSGT. In this survey, the extended model of Halpin–Tsai micromechanics is applied to determine the elastic characteristics of the composite structure. A numerical approach is employed to solve differential governing motion equations for different cases of boundary conditions. Eventually, a complete parametric study is carried out to reveal the impact of R_o/R_i, h/h_p, applied voltage, and g_{GPL} on the critical voltage response of the GPLRC microdisk integrated with PIAC.

2 GPLRC microdisk

A GPLRC microdisk and coupled with the PIAC is depicted in Fig. 1. The volume fraction for four patterns is described by a specific function as expressed follows [97]:

$$V_{GPL}(k) = V^*_{GPL} \quad \text{GPL-U} \tag{1}$$

$$V_{GPL}(k) = 2V^*_{GPL}\frac{|-1+2k-N_L|}{N_L} \quad \text{GPL-X} \tag{2}$$

$$V_{GPL}(k) = 2V^*_{GPL}\left[1-\left(\frac{|2k-N_L-1|}{N_L}\right)\right] \quad \text{GPL-O} \tag{3}$$

$$V_{GPL}(k) = 2V^*_{GPL}(2k-1)/N_L \quad \text{GPL-A} \tag{4}$$

The parameters participated in Eqs. (1–4) are introduced in Ref. [97] in detail. The explicit relation between V^*_{GPL} and g_{GPL} can be described by:

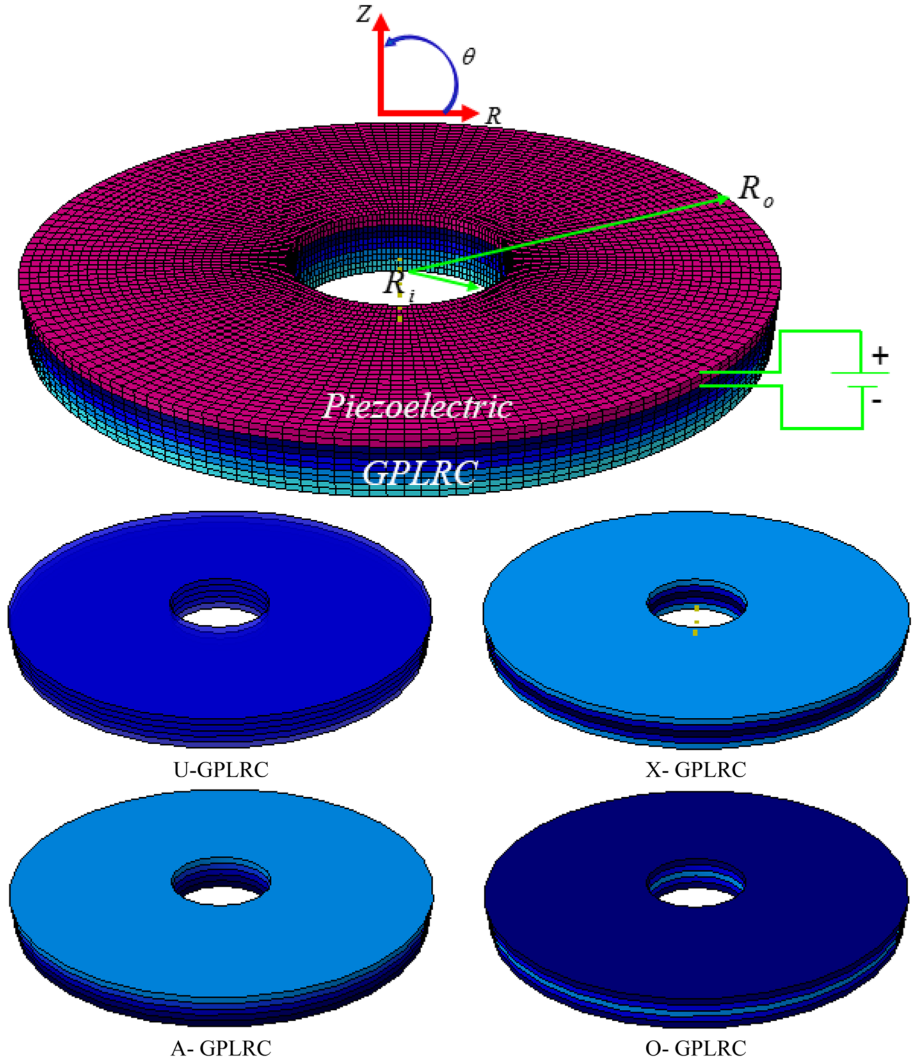

Fig. 1 GPLRC microdisk covered with piezoelectric layer

$$V^*_{\mathrm{GPL}} = \frac{g_{\mathrm{GPL}}}{g_{\mathrm{GPL}} + (\rho_{\mathrm{GPL}}/\rho_{\mathrm{m}})(1 - g_{\mathrm{GPL}})} \tag{5}$$

in which ρ_{GPL} and ρ_{m} are corresponding mass density of GPL and polymer matrix, respectively. The effective elastic modulus of the structure is approximated with the extended model of Halpin–Tsai micromechanics [98]

$$\bar{E} = \left(\frac{3}{8}\left(\frac{1 + \xi_L \eta_L V_{\mathrm{GPL}}}{1 - \eta_L V_{\mathrm{GPL}}}\right) + \frac{5}{8}\left(\frac{1 + \xi_W \eta_W V_{\mathrm{GPL}}}{1 - \eta_W V_{\mathrm{GPL}}}\right)\right) \times E_M \tag{6}$$

Also, $\xi_L = 2\frac{L_{\mathrm{GPL}}}{t_{\mathrm{GPL}}}$, $\xi_W = 2\frac{w_{\mathrm{GPL}}}{t_{\mathrm{GPL}}}$, $\eta_L = \frac{\left(E_{\mathrm{GPL}}/E_M\right)-1}{\left(E_{\mathrm{GPL}}/E_M\right)+\xi_L}$ and $\eta_W = \frac{\left(E_{\mathrm{GPL}}/E_M\right)-1}{\left(E_{\mathrm{GPL}}/E_M\right)+\xi_W}$. Finally, by utilizing the well-known rule of mixture, corresponding Poisson's ratio ν_c and mass density ρ_c of the microcomposite consisted of GNP and polymer are approximated as:

$$\bar{\nu} = \nu_{\mathrm{GPL}} V_{\mathrm{GPL}} + \nu_M V_M,$$
$$\bar{\rho} = \rho_{\mathrm{GPL}} V_{\mathrm{GPL}} + \rho_M V_M. \tag{7}$$

2.1 Displacement fields in the circular plate

HOSD theory is chosen to define the corresponding displacement fields of the GPLRC disk according to the subsequent relation [82, 83, 90, 99–111]:

$$u^c(R,z,t) = z^c u_1^c(R,t) + u_0^c(R,t) - \left[u_1^c(R,t) + \frac{\partial w_0^c(R,t)}{\partial R}\right] c_1 z^{c\,3}$$
$$v^c(R,z,t) = 0$$
$$w^c(R,z,t) = w_0^c(R,t). \tag{8}$$

Based on the conventional form of HOSDT [112–129], c_1 is equal to $4/3h^2$.

2.2 Strain–stress of core

According to HOSDT, one can formulate the strain–stress relations as follows:

$$\begin{Bmatrix} \sigma^c_{RR} \\ \sigma^c_{\theta\theta} \\ \sigma^c_{rz} \end{Bmatrix} = \begin{bmatrix} Q_{11} & Q_{12} & 0 \\ Q_{12} & Q_{22} & 0 \\ 0 & 0 & Q_{55} \end{bmatrix} \begin{Bmatrix} \varepsilon^c_{RR} - \alpha\Delta T \\ \varepsilon^c_{\theta\theta} \\ \gamma^c_{rz} \end{Bmatrix}$$
$$Q_{11} = Q_{22} = \frac{E^c}{1-\nu^{c\,2}}, \quad Q_{12} = \frac{E_c\nu_c}{1-\nu^{c\,2}}, \quad Q_{55} = \frac{E^c}{2(1+\nu^c)}, \tag{9}$$

and strain components would be written as:

$$\begin{Bmatrix} \varepsilon^c_{RR} \\ \varepsilon^c_{\theta\theta} \\ \gamma^c_{Rz} \end{Bmatrix} = \begin{bmatrix} \frac{z\partial u^c_1}{\partial R} + \frac{\partial u^c_0}{\partial R} - z^3 c_1\left(\frac{\partial u^c_1}{\partial R} + \frac{\partial^2 w^c_0}{\partial R^2}\right) \\ \frac{u^c_0}{R} + z\frac{u^c_1}{R} - z^{c\,3} c_1\left(\frac{u^c_1}{R} + \frac{\partial w^c_0}{R\partial R}\right) \\ \left(u^c_1 + \frac{\partial w^c_0}{\partial R}\right)(-3z^{c\,2}c_1 + 1) \end{bmatrix}. \tag{10}$$

2.3 Piezoelectric displacement fields

On the basis of HOSDT, the piezoelectric microdisk displacement fields can be obtained as follows:

$$\begin{aligned} u^p(R,z,t) &= z^p u^p_1(R,t) + u^p_0(R,t) - \left[\frac{\partial w^p_0(R,t)}{\partial R} + u^p_1(R,t)\right] c_1 z^{p\,3} \\ v^p(R,z,t) &= 0 \\ w^p(R,z,t) &= w^p_0(R,t). \end{aligned} \tag{11}$$

2.4 Strain–stress of piezoelectric

The corresponding stress and strain tensors of the PIACs are associated with each other according to the following equations:

$$\begin{Bmatrix} \sigma^p_{RR} \\ \sigma^p_{\theta\theta} \\ \sigma^p_{Rz} \end{Bmatrix} = \begin{bmatrix} Q_{11} & Q_{12} & 0 \\ Q_{12} & Q_{22} & 0 \\ 0 & 0 & Q_{55} \end{bmatrix} \begin{Bmatrix} \varepsilon^p_{RR} \\ \varepsilon^p_{\theta\theta} \\ \gamma^p_{Rz} \end{Bmatrix} - \begin{bmatrix} 0 & 0 & e_{31} \\ 0 & e_{32} & 0 \\ e_{15} & 0 & 0 \end{bmatrix} \begin{Bmatrix} E^p_R \\ E^p_\theta \\ E^p_z \end{Bmatrix} \tag{12}$$

$$\begin{Bmatrix} D^p_R \\ D^p_\theta \\ D^p_z \end{Bmatrix} = \begin{bmatrix} 0 & 0 & e_{15} \\ 0 & e_{22} & 0 \\ e_{31} & 0 & 0 \end{bmatrix} \begin{bmatrix} \varepsilon^p_{RR} \\ \varepsilon^p_{\theta\theta} \\ \varepsilon^p_{Rz} \end{bmatrix} + \begin{bmatrix} s_{11} & 0 & 0 \\ 0 & s_{22} & 0 \\ 0 & 0 & s_{33} \end{bmatrix} \begin{Bmatrix} E^p_R \\ E^p_\theta \\ E^p_z \end{Bmatrix} \tag{13}$$

where s_{im}, e_{mij}, and Q_{ij} in order stand for the dielectric and piezoelectric constants, and elasticity matrix. E_m and D_i indicate electric fields strength and electric displacements of the piezoelectric disk, respectively. Corresponding electric and magnetic field strength, i.e., E_x, E_θ, E_z, which are participated in Eqs. (12) and (13), would be formulated as:

$$\begin{aligned} E_R &= -\frac{\partial\tilde{\Phi}}{\partial R} \\ E_z &= -\frac{\partial\tilde{\Phi}}{\partial z}. \end{aligned} \tag{14}$$

Wang [130] explored that the electric potential ($\Phi(x,\theta,z,t)$) can be accounted as:

$$\Phi(R,z,t) = \frac{2z\phi_0}{h} - \phi(R,t)\cos(\beta z) \tag{15}$$

in which $\beta = \pi/h$ and ϕ_0 stands for the initial external electric.

2.5 E-compatibility equations

Following relations present mathematical expression for the conditions of compatibility taking perfect bonding between the core and PIAC section and taken into consideration at $z_{\mathrm{p}} = -h_{\mathrm{p}}/2$:

$$\begin{aligned} u^c|_{z_c=h_c/2} &= u^p|_{z_{\mathrm{p}}=-h_{\mathrm{p}}/2}, \\ w^c|_{z_c=h_c/2} &= w^p|_{z_{\mathrm{p}}=-h_{\mathrm{p}}/2}. \end{aligned} \tag{16}$$

Based on Eq. (16), the displacement-dependent parameters are related to each other in the PIAC as follows:

$$\begin{aligned} &c_1\left(\frac{-h^c}{2}\right)^3\left[\frac{\partial w^c_0}{\partial R}\right] + c_1\left(\frac{h^p}{2}\right)^3\left[+\frac{\partial w^p_0}{\partial R}\right] \\ &\quad = u^p_0 - u^c_0 + u^c_1\left[c_1\left(\frac{h^c}{2}\right)^3 - \frac{h^c}{2}\right] - u^p_1\left[c_1\left(\frac{h^p}{2}\right)^3 + \frac{h^p}{2}\right], \\ &w^c_0 = w^p_0. \end{aligned} \tag{17}$$

2.6 Extended Hamilton's principle

In order to acquire the governing equations and related boundary conditions, we can utilize Hamilton's principle as follows:

$$\int_{t_1}^{t_2} (\delta U^i - \delta W^i)\mathrm{d}t = 0 \qquad i = c, p \tag{18}$$

the following relation describes the components involved in the process of obtaining the strain energy of the aforementioned microdisk:

$$\delta U^c = \frac{1}{2}\iiint\limits_V \sigma_{ij}^c \delta\varepsilon_{ij}^c \mathrm{d}V = \int \left[\begin{array}{l} \left[N_{RR}^c \frac{\partial \delta u_0^c}{\partial R^c} + M_{RR}^c \frac{\partial \delta u_1^c}{\partial R^c} - P_{RR}^c c_1 \left(\frac{\partial \delta u_1^c}{\partial R^c} + \frac{\partial^2 \delta w_0^c}{\partial R^{c2}} \right)\right] \\ + \left[N_{\theta\theta}^c \frac{\delta u_0^c}{R^c} + M_{\theta\theta}^c \frac{\delta u_1^c}{R^c} - P_{\theta\theta}^c c_1 \left(\frac{\delta u_1^c}{R^c} + \frac{\partial \delta w_0^c}{R \partial R^c} \right)\right] \\ + \left[(Q_{Rz}^c - 3S_{Rz}^c c_1)\left(\delta u_1^c + \frac{\partial \delta w_0^c}{\partial R^c} \right)\right] \end{array} \right] \mathrm{d}R \tag{19}$$

$$\begin{aligned} \delta U^p &= \frac{1}{2}\iiint\limits_V \sigma_{ij}^p \delta\varepsilon_{ij}^p \mathrm{d}V - \iiint\limits_{V_{\text{piezolayer}}} (D_R^p \delta E_R^p + D_z^p \delta E_z^p)\mathrm{d}V_{\text{piezolayer}} \\ &= \int \left[\begin{array}{l} \left[N_{RR}^p \frac{\partial \delta u_0^p}{\partial R^p} + M_{RR}^p \frac{\partial \delta u_1^p}{\partial R^p} - P_{RR}^p c_1 \left(\frac{\partial \delta u_1^p}{\partial R^p} + \frac{\partial^2 \delta w_0^p}{\partial R^{p2}} \right)\right] \\ + \left[N_{\theta\theta}^p \frac{\delta u_0^p}{R^p} + M_{\theta\theta}^p \frac{\delta u_1^p}{R^p} - P_{\theta\theta}^p c_1 \left(\frac{\delta u_1^p}{R^p} + \frac{\partial \delta w_0^p}{R^p \partial R^p} \right)\right] \\ + \left[(Q_{Rz}^p - 3S_{Rz}^p c_1)\left(\delta u_1^p + \frac{\partial \delta w_0^p}{\partial R^p} \right)\right] \end{array} \right] \mathrm{d}R^p \\ &\quad - \int_0^{2\pi} \int_{R_i}^{R_o} \int_{-h_p/2}^{h_p/2} \left[\begin{array}{c} D_R^p \left\{ \cos(\beta z) \frac{\partial}{\partial R^p} \delta\phi \right\} \\ -D_z^p (\beta \sin(\beta z) \delta\phi) \end{array} \right] R \mathrm{d}R \mathrm{d}\theta \end{aligned} \tag{20}$$

where

$$\begin{aligned} &\int_z \left\{ \sigma_{RR}^i, z\sigma_{RR}^i, z^3 \sigma_{RR}^i \right\} \mathrm{d}z = \left\{ N_{RR}^i, M_{RR}^i, P_{RR}^i \right\} = ; \quad i = c, p \\ &\int_z \left\{ \sigma_{\theta\theta}^i, z\sigma_{\theta\theta}^i, z^3 \sigma_{\theta\theta}^i \right\} \mathrm{d}z = \left\{ N_{\theta\theta}^i, M_{\theta\theta}^i, P_{\theta\theta}^i \right\} = ; \\ &\int_z \left\{ \sigma_{Rz}^i, z^2 \sigma_{Rz}^i \right\} \mathrm{d}z = \left\{ Q_{Rz}^i, S_{Rz}^i \right\} = ; \end{aligned} \tag{21}$$

The first variation of the external work applied by an external electrical load to the structure can be obtained as follows [51]:

$$W_1 = \frac{1}{2} \int\limits_z \left[(N_i^P) w_{,x}^2 \right] \mathrm{d}R, \quad i = 1, 2 \tag{22}$$

where N_i^P represents the external electric load which could be acquired as follows:

$$N_i^P = -2\left(e_{31} - \frac{c_{13} e_{33}}{c_{33}} \right) \phi_0. \tag{23}$$

Eventually, differential equations of motion of the microstructure are extracted as follows:

$$\begin{aligned} &\delta u_0^i : \\ &\quad \frac{\partial N_{RR}^i}{\partial R} - \frac{N_{\theta\theta}^i}{R} = 0, \\ &\delta w_0^i : \\ &\quad c_1 \frac{\partial^2 P_{RR}^i}{\partial R^{i2}} - c_1 \frac{\partial P_{\theta\theta}^i}{R^i \partial R^i} + \frac{\partial Q_{Rz}^i}{\partial R^i} - 3c_1 \frac{\partial S_{Rz}^i}{\partial R^i} - N_1^p w_{0,x^2}^i = 0, \\ &\delta u_1^i : \\ &\quad \frac{\partial M_{RR}^i}{\partial R^i} - \frac{\partial P_{RR}^i}{\partial R^i} c_1 - \frac{M_{\theta\theta}^i}{R^i} + \frac{P_{\theta\theta}^i c_1}{R^i} - Q_{Rz}^i + 3S_{Rz}^i c_1 = 0, \\ &\delta\phi : \\ &\quad -(X_{11} - 3X_{12})\left(u_1^p \frac{\partial}{\partial R^p} \delta\phi + \frac{\partial w_0^p}{\partial R^p} \frac{\partial}{\partial R^p} \delta\phi \right) \\ &\quad + \frac{\partial}{\partial R^p} \delta\phi X_{41} \partial\phi / \partial R^p \\ &\quad + \left(X_{31} \frac{\partial u_0^p}{\partial R} \delta\phi + X_{32} \frac{\partial u_1^p}{\partial R} \delta\phi - X_{33} \left(\frac{\partial u_1^p}{\partial R} \delta\phi + \frac{\partial^2 w_0^p}{\partial R^2} \delta\phi \right) \right) + X_{42} \phi \delta\phi = 0, \quad i = c, p \end{aligned} \tag{24}$$

where

$$
\begin{aligned}
N^i_{RR} &= \left[A^i_{11}\frac{\partial u^i_0}{\partial R^i} + B^i_{11}\frac{\partial u^i_1}{\partial R^i} - D^i_{11}c_1\left(\frac{\partial u^i_1}{\partial R^i} + \frac{\partial^2 w^i_0}{\partial R^{i2}}\right)\right] + \left[A^i_{12}\frac{u^i_0}{R^i} + B^i_{12}\frac{u_1}{R} - D^i_{12}c_1\left(\frac{u^i_1}{R^i} + \frac{\partial w^i_0}{R^i\partial R^i}\right)\right] \\
&\quad - X_{31}\phi \\
M^i_{RR} &= \left[B^i_{11}\frac{\partial u^i_0}{\partial R^i} + C^i_{11}\frac{\partial u^i_1}{\partial R^i} - E^i_{11}c_1\left(\frac{\partial u^i_1}{\partial R^i} + \frac{\partial^2 w^i_0}{\partial R^{i2}}\right)\right] + \left[B^i_{12}\frac{u^i_0}{R^i} + C^i_{12}\frac{u^i_1}{R^i} - E^i_{12}c_1\left(\frac{u^i_1}{R^i} + \frac{\partial w^i_0}{R^i\partial R^i}\right)\right] \\
&\quad - X_{32}\phi \\
P^i_{RR} &= \left[D^i_{11}\frac{\partial u^i_0}{\partial R^i} + E^i_{11}\frac{\partial u^i_1}{\partial R^i} - G^i_{11}c_1\left(\frac{\partial u^i_1}{\partial R^i} + \frac{\partial^2 w^i_0}{\partial R^{i2}}\right)\right] + \left[D^i_{12}\frac{u^i_0}{R^i} + E^i_{12}\frac{u^i_1}{R^i} - G^i_{12}c_1\left(\frac{u^i_1}{R^i} + \frac{\partial w^i_0}{R^i\partial R^i}\right)\right] \\
&\quad - X_{33}\phi \\
N^i_{\theta\theta} &= \left[A^i_{12}\frac{\partial u^i_0}{\partial R^i} + B^i_{12}\frac{\partial u^i_1}{\partial R^i} - D^i_{12}c_1\left(\frac{\partial u^i_1}{\partial R^i} + \frac{\partial^2 w^i_0}{\partial R^{i2}}\right)\right] + Q^i_{22}\left[A^i_{22}\frac{u^i_0}{R^i} + B^i_{22}\frac{u^i_1}{R^i} - D^i_{22}c_1\left(\frac{u^i_1}{R^i} + \frac{\partial w^i_0}{R^i\partial R^i}\right)\right] \\
M^i_{\theta\theta} &= \left[B^i_{12}\frac{\partial u^i_0}{\partial R^i} + C^i_{12}\frac{\partial u^i_1}{\partial R^i} - E^i_{12}c_1\left(\frac{\partial u^i_1}{\partial R^i} + \frac{\partial^2 w^i_0}{\partial R^{i2}}\right)\right] + Q^i_{22}\left[B^i_{22}\frac{u^i_0}{R^i} + C^i_{22}\frac{u^i_1}{R^i} - E^i_{22}c_1\left(\frac{u^i_1}{R^i} + \frac{\partial w^i_0}{R^i\partial R^i}\right)\right] \\
P^i_{\theta\theta} &= \left[D^i_{12}\frac{\partial u^i_0}{\partial R^i} + E^i_{12}\frac{\partial u^i_1}{\partial R^i} - G^i_{12}c_1\left(\frac{\partial u^i_1}{\partial R^i} + \frac{\partial^2 w^i_0}{\partial R^{i2}}\right)\right] + Q^i_{22}\left[D^i_{22}\frac{u^i_0}{R^i} + E^i_{22}\frac{u^i_1}{R^i} - G^i_{22}c_1\left(\frac{u^i_1}{R^i} + \frac{\partial w^i_0}{R^i\partial R^i}\right)\right] \\
Q^i_{Rz} &= (A^i_{55} - 3C^i_{55}c_1)\left(u^i_1 + \frac{\partial w^i_0}{\partial R^i}\right) + X_{11}\partial\phi/\partial R^i \\
S^i_{Rz} &= (C^i_{55} - 3E^i_{55}c_1)\left(u^i_1 + \frac{\partial w^i_0}{\partial R^i}\right) + X_{12}\partial\phi/\partial R^i; \quad i = c, p
\end{aligned}
\tag{25}
$$

and

$$
\left[A^i_{ij}, B^i_{ij}, C^i_{ij}, D^i_{ij}, E^i_{ij}, F^i_{ij}, G^i_{ij}\right] = \int_{-h/2}^{h/2} Q_{ij}\left[1, z^i, z^{i2}, z^{i3}, z^{i4}, z^{i5}, z^{i6}\right]\mathrm{d}z; \quad i = c, p \tag{26}
$$

Moreover, the parameters involved in the equation of the PIAC can be given as follows:

$$
\begin{aligned}
X_{11} &= \int e_{15}\cos(\beta z), \quad X_{12} = \int e_{15}z^2 c_1\cos(\beta z), \\
X_{31} &= \int \beta e_{31}\sin(\beta z), \\
X_{32} &= \int z\beta e_{31}\sin(\beta z), \quad X_{33} = \int z^3 c_1\beta e_{31}\sin(\beta z), \\
X_{41} &= \int s_{11}(\cos(\beta z))^2, \quad X_{42} = \int s_{33}(\beta\sin(\beta z))^2
\end{aligned}
\tag{27}
$$

It should be noticed that based on the compatibility relation (Eq. 16), the number of corresponding unknown variables of the core is declined from 5 to 3. Thus, the total number of unknowns in the piezoelectric face sheet and the GPLRC core is reduced to 8.

2.7 NSG theory

In the present article, the size-dependent effects are captured in the mathematical model through NSG theory. According to the theory, corresponding stain and stress tensors of microstructure are correlated with each order as follows:

$$
(1 - \mu^2\nabla^2)t^i_{ij} = C^i_{ijck}(1 - l^2\nabla^2)\varepsilon^i_{ck}; \quad i = c, p \tag{28}
$$

where $\nabla^2 = \partial^2/\partial\theta^2 + \partial/R\partial\theta$, C_{ijck}, ε_{ck}, and t_{ij} are tensors of elasticity, strain, and stress of NSGT, respectively. According to NSGT, the tensor of stress would be presented by the subsequent relation [43]:

$$
t^i_{ij} = \sigma^i_{ij} - \nabla\sigma^{i(1)}_{ij}; \quad i = c, p \tag{29}
$$

Based on Eq. (29), the extended form of the relation between stress and strain would be expressed as follows [131]:

$$(1-\mu^2\nabla^2)\begin{Bmatrix} t^i_{RR} \\ t^i_{\theta\theta} \\ t^i_{Rz} \end{Bmatrix} = (1-l^2\nabla^2)\begin{bmatrix} Q_{11} & Q_{12} & 0 \\ Q_{12} & Q_{22} & 0 \\ 0 & 0 & Q_{55} \end{bmatrix}\begin{Bmatrix} \varepsilon^i_{rr} - \alpha\Delta T \\ \varepsilon^i_{\theta\theta} \\ \gamma^i_{rz} \end{Bmatrix}; \quad i = c, p \tag{30}$$

Thus, the governing differential equations of motion of the microdisk in thermal environment joint with the PIAC are derived as follows:

$$\begin{aligned}
&\delta u^i_0 : \\
&\quad (1-l^2\nabla^2)\left[\frac{\partial N^i_{RR}}{\partial R} - \frac{N^i_{\theta\theta}}{R}\right] = 0, \\
&\delta w^i_0 : \\
&\quad (1-l^2\nabla^2)\left[c_1\frac{\partial^2 P^i_{RR}}{\partial R^{i2}} - c_1\frac{\partial P^i_{\theta\theta}}{R^i\partial R^i} + \frac{\partial Q^i_{Rz}}{\partial R^i} - 3c_1\frac{\partial S^i_{Rz}}{\partial R^i} - N^p_1 w^i_{0,x^2}\right] = 0, \\
&\delta u^i_1 : \\
&\quad (1-l^2\nabla^2)\left[\frac{\partial M^i_{RR}}{\partial R^i} - \frac{\partial P^i_{RR}}{\partial R^i}c_1 - \frac{M^i_{\theta\theta}}{R^i} + \frac{P^i_{\theta\theta}c_1}{R^i} - Q^i_{Rz} + 3S^i_{Rz}c_1\right] = 0, \\
&\delta\phi : \\
&\quad (1-l^2\nabla^2)\begin{pmatrix} +X_{31}\dfrac{\partial u^p_0}{\partial R^p} + (X_{11}-3X_{12})\dfrac{\partial^2 w^p_0}{\partial R^{p2}} - X_{33}\dfrac{\partial^2 w^p_0}{\partial R^{p2}} \\ -(-X_{11}+3X_{12})\dfrac{\partial u^p_1}{\partial R^p} + X_{32}\dfrac{\partial u^p_1}{\partial R^p} - X_{33}\dfrac{\partial u^p_1}{\partial R^p} \\ -X_{41}\dfrac{\partial^2\phi}{\partial R^{p2}} + X_{42}\phi \end{pmatrix} = 0; \quad i = c, p
\end{aligned} \tag{31}$$

Table 1 The effect of the number of grid points on the results convergence for the critical voltage of the GNPRC microdisk with respect to different piezoelectric thickness and boundary conditions (B. Cs) when $R_o/R_i = 1.3$, $h/R = 0.1$, $l = R/10$, pattern 1

B. Cs	h_p/h	$N=9$	$N=11$	$N=13$	$N=15$	$N=17$	$N=19$
S–S	0	38.10933	37.99989	37.89160	37.782388	37.72372	37.713261
	0.05	42.56944	42.415034	42.26195	42.109183	42.08659	42.079991
	0.1	45.15809	44.973400	44.791203	44.612032	44.59265	44.589659
	0.15	47.97213	47.765279	47.562300	47.363099	47.34256	47.336598
	0.2	52.30575	52.072106	51.843569	51.619029	51.58658	51.578963
C–S	0	61.70749	61.938951	62.168790	62.386126	62.009457	62.008965
	0.05	76.55290	76.776339	77.000004	77.216890	77.009236	77.015658
	0.1	85.51214	85.705416	86.106898	86.106898	86.108963	86.109658
	0.15	93.06857	93.256267	93.660638	93.660638	93.745623	93.754698
	0.2	102.7425	102.94342	103.38185	103.38185	103.60635	103.61569
C–C	0	94.222794	93.919629	93.943282	93.93402	93.945632	93.945698
	0.05	126.61913	126.45657	126.41456	126.46459	126.45653	126.45659
	0.1	147.63284	147.44263	147.33826	147.35698	147.36598	147.34658
	0.15	163.87048	163.67296	163.55759	163.54569	163.55698	163.55985
	0.2	182.46380	182.27309	182.16256	182.15895	182.15365	182.15659

Table 2 Comparison of obtained dynamic response for different h/R_o and boundary conditions with the result of Ref [79]

h/R_o	Mode number = 1 (Ref [79])	Mode number = 1 (present)	Mode number = 2 (Ref [79])	Mode number = 2 (present)	Mode number = 3 (Ref [79])	Mode number = 3 (present)	Mode number = 4 (Ref [79])	Mode number = 4 (present)
Simply–simply boundary conditions								
0.001	27.280	27.621156	75.364	76.137500	148.21	149.25865	245.47	246.72681
0.05	26.534	27.139571	71.228	71.934144	135.24	138.23412	215.08	218.86644
0.1	24.629	25.471425	62.140	61.888783	111.12	113.50531	167.16	169.44431
0.15	22.230	22.903314	52.762	52.671618	90.286	93.677721	131.35	132.25517
Clamped–simply boundary conditions								
0.001	34.609	35.288408	95.738	96.8504221	188.14	189.473448	311.40	312.880757
0.05	33.533	34.121372	89.550	89.8115866	168.60	169.062419	265.78	265.572010
0.1	30.841	31.223430	76.560	75.9270209	134.71	134.658209	200.02	201.008081
0.15	27.545	27.717438	63.827	63.3132404	107.32	108.095118	154.20	158.820998
Clamped–clamped boundary conditions								
0.001	59.819	62.421081	198.04	202.74802	415.12	417.733480	711.12	715.369157
0.05	57.250	59.724417	177.84	180.65834	344.35	346.333165	541.41	536.508525
0.1	51.219	53.472342	142.71	144.05551	252.22	257.196138	369.86	368.652369
0.15	44.443	45.565987	114.18	116.17581	192.05	190.569853	272.49	271.256987

Table 3 Material properties of the epoxy and GPL [80]

Material properties	Epoxy	GNP
Young's modulus (GPa)	3	1010
Density (kg m^{-3})	1200	1062.5
Poisson's ratio	0.34	0.186
Thermal expansion coefficient(10^{-6}/K)	60	5

Eventually, the related boundary conditions would be formulated as follows:

$$\begin{aligned}
&\delta u_0^i = 0 \text{ or } (1 - l^2\nabla^2)\left(N_{RR}^i\right)n_R^i\\
&\delta w_0^i = 0 \text{ or } (1 - l^2\nabla^2)\\
&\left(-P_{RR}^i c_1 + c_1\frac{\partial P_{RR}^i}{\partial R^i} - \frac{P_{\theta\theta}^i c_1}{R^i} + (Q_{Rz}^i - 3S_{Rz}^i c_1)\right)n_R^i, \quad i = c, p\\
&\delta u_1^i = 0 \text{ or } (1 - l^2\nabla^2)\left(M_{RR}^i - P_{RR}^i c_1\right)n_R^i,\\
&\delta\phi = 0
\end{aligned} \tag{32}$$

The governing equations of the smart microstructure are presented in the Appendix section.

Table 4 Material properties of piezoelectric layer which is composed of $BiTiO_3$–$CoFe_2O_4$ [81]

Material constants	$BiTiO_3$–$CoFe_2O_4$
Elastic (GPa)	$c_{11} = 226,\ c_{12} = 125,\ c_{13} = 124,\ c_{33} = 216,\ c_{44} = 44.2,\ c_{55} = 44.2,\ c_{66} = 50.5$
Piezoelectric (C m^{-2})	$e_{31} = -2.2,\ e_{33} = 9.3,\ e_{15} = 5.8$
Dielectric (10^{-9} C V m^{-1})	$s_{11} = 5.64,\ s_{22} = 5.64,\ s_{33} = 6.35$
Piezomagnetic (N A m^{-1})	$q_{15} = 275,\ q_{31} = 290.1,\ q_{33} = 349.9$
Magnetic (10^{-6} Ns^2 C^{-2})	$r_{11} = -297,\ r_{33} = 83.5$
Thermal moduli (10^5 N km^{-2})	$\beta_1 = 4.74,\ \beta_3 = 4.53$
Pyroelectric (10^{-6} C N^{-1})	$P_3 = 25$
Mass density (10^3 kg m^{-3})	$\rho = 5.55$

2.8 Solution procedure

In order to explore the vibration performance of the microdisk in this survey, a numerical solution approach based on the well-known GDQM is followed. According to this method, the nth-order derivatives of a smooth function f would be obtained by the following expression [132]:

$$\frac{\partial^n f}{\partial R^n} = \sum_{m=1}^{M} C_{j,m}^{(n)} f_{m,k} \tag{33}$$

The weighting coefficients associated with nth-order derivative along the radius direction is defined as $C^{(n)}$. From Eq. (33), it is apparent that calculating the weighting coefficients is the essential parts of DQM. To estimate the nth-order derivatives of function along radius direction, two forms of DQM developed of GDQM are adopted in this study. Thus, the weighting coefficients are computed from the first-order derivative which is shown as

$$\begin{aligned} C_{ij}^{(1)} &= \frac{M(x_i)}{(x_i - x_j)M(x_j)} \quad && i,j = 1,2,\ldots,n \\ & && i \neq j \\ C_{ij}^{(1)} &= -\sum_{j=1,i\neq j}^{n} C_{ij}^{(1)} && i = j \end{aligned} \tag{34}$$

here,

$$M(x_i) = \prod_{j=1,j\neq i}^{n} (x_i - x_j) \tag{35}$$

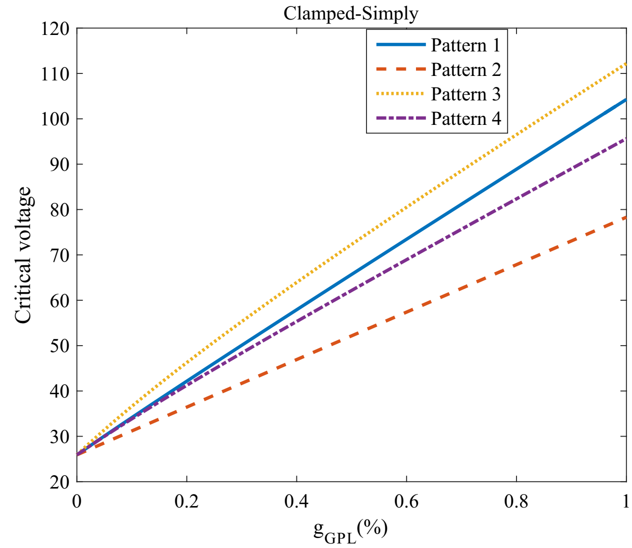

Fig. 3 Effects of different values and various distribution patterns of the GPL on the critical voltage of the GPLRC microdisk covered with a piezoelectric layer for clamped–simply boundary conditions

Likewise, the weighting coefficients for higher-order derivatives can be calculated using the shown expressions.

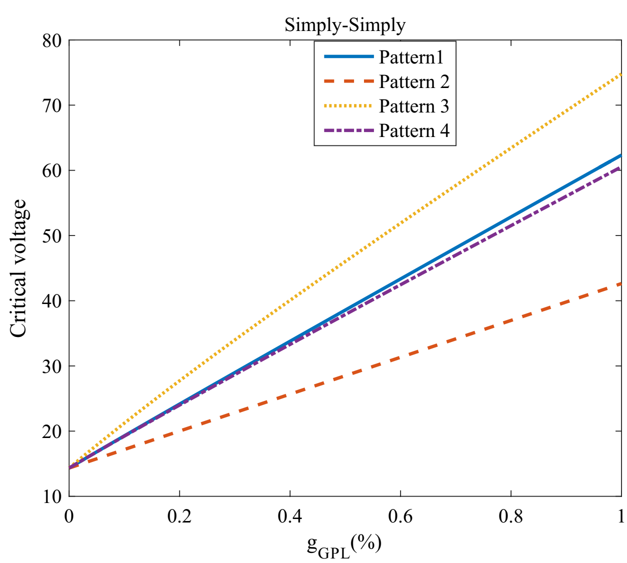

Fig. 2 Effects of different values and various distribution patterns of the GPL on the critical voltage of the GPLRC microdisk covered with a piezoelectric layer for simply–simply boundary conditions

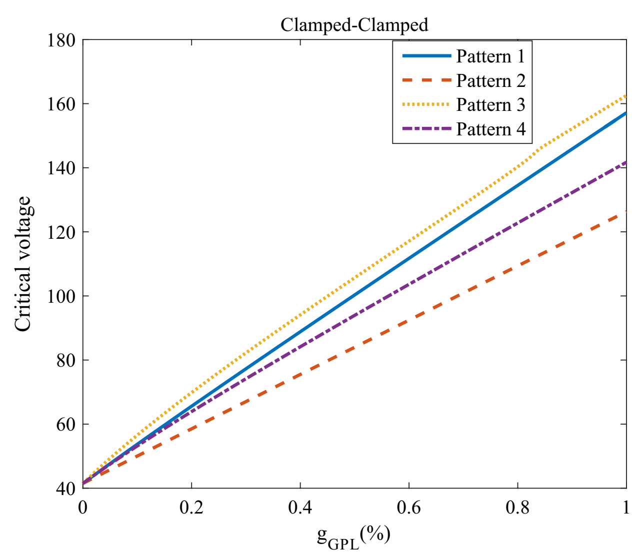

Fig. 4 Effects of different values and various distribution patterns of the GPL on the critical voltage of the GPLRC microdisk covered with a piezoelectric layer for clamped–clamped boundary conditions

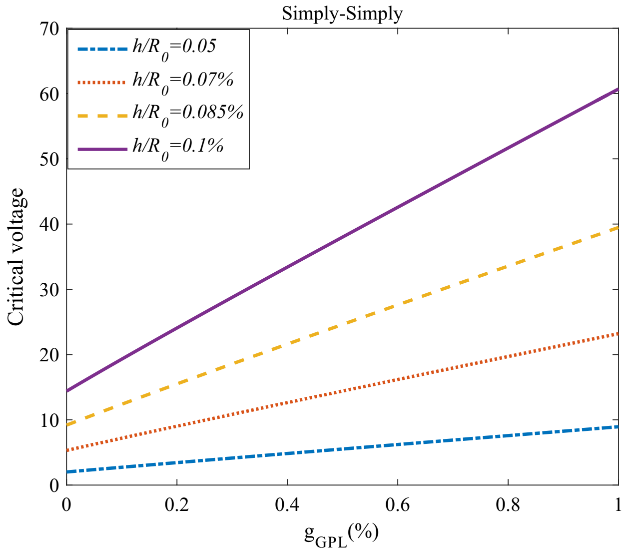

Fig. 5 Effects of different values of g_{GPL} and h/R_{o} on the critical voltage of the GPLRC microdisk covered with a piezoelectric sensor for simply–simply boundary conditions

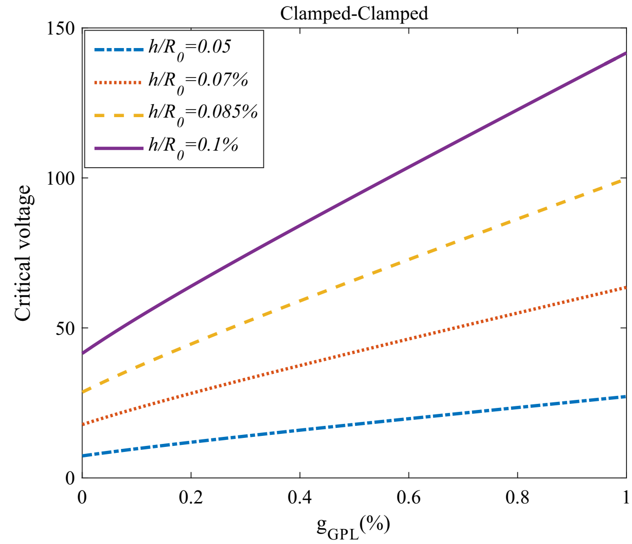

Fig. 7 Effects of different values of g_{GPL} and h/R_{o} on the critical voltage of the GPLRC microdisk covered with a piezoelectric sensor for clamped–clamped boundary conditions

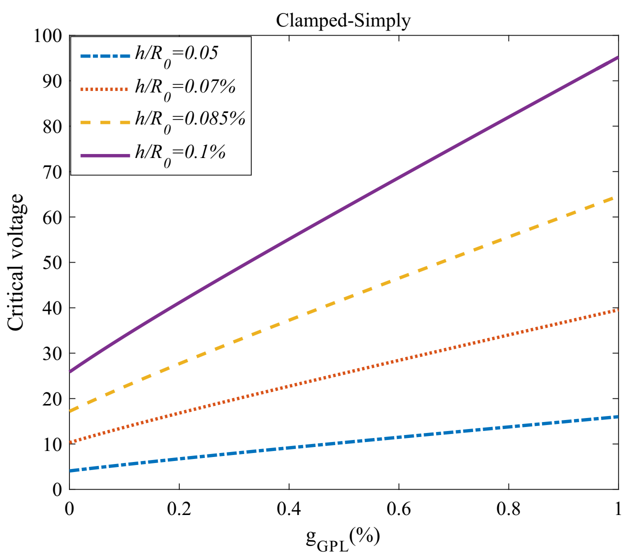

Fig. 6 Effects of different values of g_{GPL} and h/R_{o} on the critical voltage of the GPLRC microdisk covered with a piezoelectric sensor for clamped–simply boundary conditions

$$
\begin{aligned}
&C_{ij}^{(r)} = r\left[C_{ij}^{(r-1)}C_{ij}^{(1)} - \frac{C_{ij}^{(r-1)}}{\left(x_i - x_j\right)}\right]\\
&i,j = 1,2,\ldots,n,\ \ i \neq j\\
&\text{and}\\
&2 \le r \le n-1\\
&C_{ii}^{(r)} = -\sum_{j=1, i\neq j}^{n} C_{ij}^{(r)}\\
&i,j = 1,2,\ldots,n\\
&\text{and}\\
&1 \le r \le n-1
\end{aligned}
\tag{36}
$$

Currently, in this research, a non-uniform batch of seeds is chosen in r axis which is shown as:

$$
\begin{aligned}
&r_i = \frac{R_0 - R_i}{2}\left(-\cos\left((i-1)/\left(N_i - 1\right)\pi\right) + 1\right) + R_i\\
&\quad i = 1,2,3,\ldots,N_i
\end{aligned}
\tag{37}
$$

Considering the linear motion equations of the structure, we can obtain the total stiffness as follows:

$$
\left\{\begin{bmatrix} \left[K_{dd}\right] & \left[K_{db}\right] \\ \left[K_{bd}\right] & \left[K_{bb}\right] \end{bmatrix}\right\}\begin{Bmatrix} \delta_d \\ \delta_b \end{Bmatrix} = 0 \tag{38}
$$

Table 5 Effect of different values of the R_o/h and l/h parameters on the static response of the smart microcircular plate

	Pure epoxy	Pattern 1	Pattern 2	Pattern 3	Pattern 4
$l=0$					
$R_o/h=15$	14.391014	38.6950945	28.60415145	46.14308691	37.99989882
$R_o/h=20$	8.4826402	23.41557031	16.78335526	28.99959924	22.98010877
$R_o/h=25$	5.4870839	15.35638353	10.82586309	19.42324934	15.08444849
$l/h=10$					
$R_o/h=15$	14.6283085	39.01263973	28.76188551	46.75587503	39.66600735
$R_o/h=20$	8.57571202	23.55226797	16.85536175	29.24298815	23.52799920
$R_o/h=25$	5.53671659	15.43225670	10.86682202	19.55430072	15.32931969

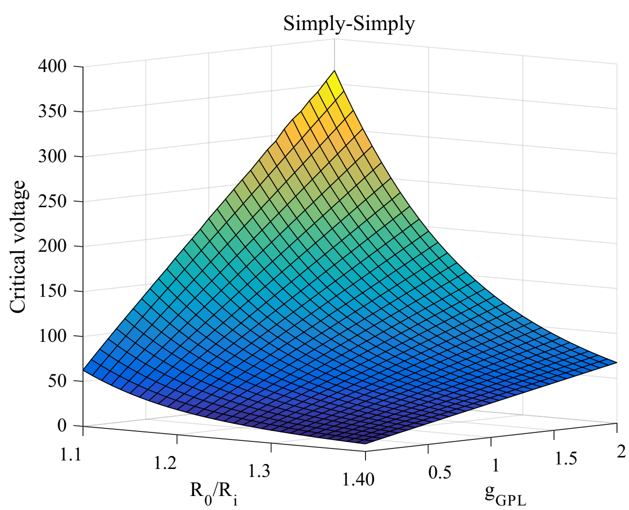

Fig. 8 Effects of g_{GPL} and R_o/R_i parameters on the critical voltage of the GPLRC microdisk covered with piezoelectric sensor for simply–simply boundary conditions

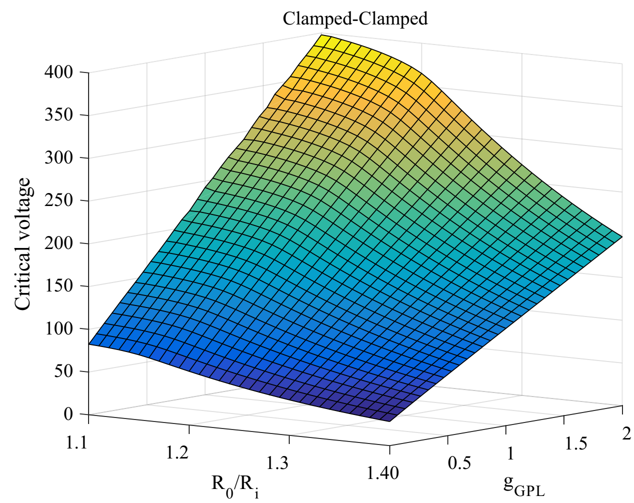

Fig. 10 Effects of g_{GPL} and R_o/R_i parameters on the critical voltage of the GPLRC microdisk covered with piezoelectric sensor for clamped–clamped boundary conditions

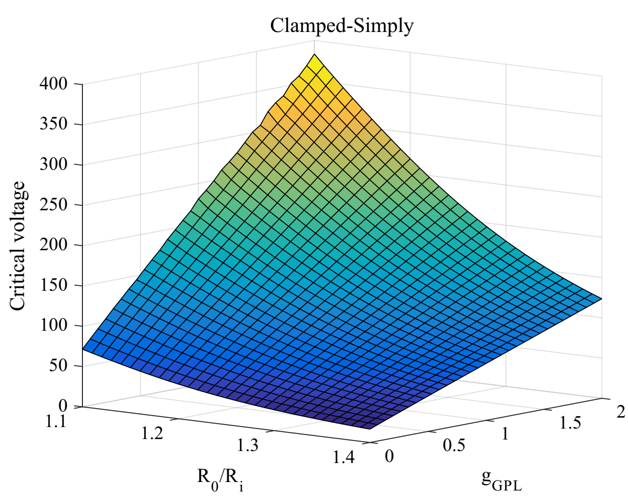

Fig. 9 Effects of g_{GPL} and R_o/R_i parameters on the critical voltage of the GPLRC microdisk covered with piezoelectric sensor for clamped–simply boundary conditions

where the subscripts b and d represent the boundary and domain grid points, respectively. Moreover, δ denotes the vector of displacements. Equation (38) would be transformed into a standard form of eigenvalue problem:

$$[K^*]\{\delta_i\} = 0,$$
$$[K^*] = [K_{dd} - K_{db}K_{bb}^{-1}K_{bd}] \tag{39}$$

2.9 Convergencey

A sufficient number of elements and grid points are essential for obtaining the accurate results in FEM and GDQM [55–59, 133–145]. To guarantee an acceptable accuracy in the results of GDQM, it is crucial to find a sufficient number of grid points. Accordingly, the convergence study is performed for different cases of boundary conditions and also h_p/h ratio. As shown in Table 1, $N=17$ as the number of grid points can provide the sufficient accuracy of GDQM results.

2.10 Validation

Numerical results from Table 3, for an isotropic circular plate and different geometrical parameters, were varied with those Ref. [146], to examine the efficiency and validity approach for this study. The maximal discrepancy, as entailed by the reconciliation reported in the table, is relatively 1% (Table 2).

3 Results

A GPL with a thickness of h_{GNP}= 1.5 nm and radius of R_{GNP} = 0.75 µm is used and presented in Table 3. It should be mentioned that the corresponding properties of piezoelectric material are provided in Table 4.

Figures 2, 3, and 4 show g_{GPL} and GPLRC pattern's effects on the critical voltage of the microdisk under various boundary conditions.

As a typical result which can label Figs. 2, 3, and 4, for S–S, C–S, and C–C boundary conditions and each GPLRC pattern, there is a direct or positive effect from on the critical voltage of the smart microdisk. According to these figures, the best pattern of the GPRC microdisk for having the highest critical voltage at all ranges of the parameter is pattern 3. For all patterns, the relation between parameter and critical voltage is linear, and when the boundary conditions are considered S–S, patterns 4 and 1 have not shown any effect on the critical voltage of the structure. As an astonishing result from Figs. 2, 3, and 4, when the boundary conditions change from S–S to C–C, the influence of GPL pattern on the critical voltage of the smart circular structure in all ranges of the parameter decreases.

Figures 5, 6, and 7 show the effects of different values of g_{GPL} and h/R_o parameters on the critical voltage of the smart microdisk.

Accordion to Figs. 5, 6, and 7, for a specific value of the h/R_o parameter and all boundary conditions, by increasing the value of the g_{GPL}, critical voltage of the structure increases linearly. As an astonishing result for the literature, there is a positive and direct relation between h/R_o and critical voltage of the structure. As a conclusion from Figs. 5, 6, and 7, when the rigidity of the structure increased, the influences of the h/R_o parameter on the critical voltage decrease. Besides, having an exact glance to these figures can find out an interesting result which as well as the positive effect from g_{GPL} on the critical voltage, by increasing g_{GPL} the positive impact of h/R_o parameter on the critical voltage of the structure has been intensified. For greater g_{GPL} parameter, the effect of h/R_o parameter on the critical voltage is more significant in comparison with at the lower value of it.

The main point of Table 5 is a presentation about the influences of the length scale (l/h) and R_o/h parameters on the critical voltage of the simply supported microcircular plate covered with a piezoelectric sensor. According to Table 5, as well as an indirect effect from R_o/h parameter on the frequency, increasing the length scale parameter encounters the structure with a weakness in the dynamic stability of the structure. By having an exact glance at Table 5, the negative effect from R_o/h on the critical voltage of the smart circular plate is much more remarkable in comparison with the same impact from the length scale parameter on the natural property of the structure. As a useful suggestion for applied nanoindustries, by dedicating exact attention to Table 5 can conclude that the highest critical voltage of the composite microdisk is seen when the GPLRC pattern is considered as pattern 1. More on this research, Figs. 8, 9, and 10 have an interview about the impacts of the g_{GPL} and R_o/R_i parameters on the critical voltage of the smart GPLRC microdisk. Correspondent to Figs. 8, 9, and 10, it would be a relevant result which both of g_{GPL} and R_o/R_i parameters have an enhancing effect on the static response or critical voltage of the microstructure. It is evident that the relation between g_{GPL} and critical voltage is direct and linear. In contrast, the relation between R_o/R_i and critical voltage is exponential, polynomial, and exponential for S–S, C–C, and C–S. For more comprehensive, it would be a useful suggestion for the literature, and by increasing the R_o/R_i, critical voltage of the smart structure increases more intensely in comparison with the g_{GPL}.

4 Conclusion

For the first time, electrically responses of a GPLRC-reinforced microdisk covered with PIAC were explored using the GDQ method and NSG theory. The compatibility conditions were extracted by assuming perfect bonding at the contact interface of the PIAC and the core. Also, the piezoelectricity of the face sheet is modeled with the aid of Maxwell's equation. The results displayed that ΔT, R_o/R_i, different patterns of GPLs, and g_{GPL} have significant impact on the critical voltage responses of the GPLRC microdisk. The main results are that:

- Changing from S–S to C–C, the influence of GPL pattern on the critical voltage decreases.
- At the greater g_{GPL} parameter, the effect of h/R_o parameter on the critical voltage is more significant in comparison with the lower value of it.
- By increasing the h_p/h, the critical voltage of the GPLRC microdisk covered with PIAC increases.
- By increasing R_o/R_i, the critical voltage of the smart structure increases more intensely in comparison with the g_{GPL}.

Appendix

The governing equations of the structure are presented as follows:

δu_0^i :

$$(1-l^2\nabla^2)\left[\begin{array}{l}\frac{\partial}{\partial R}\left(\begin{array}{l}\left[A_{11}^i\frac{\partial u_0^i}{\partial R^i}+B_{11}^i\frac{\partial u_1^i}{\partial R^i}-D_{11}^ic_1\left(\frac{\partial u_1^i}{\partial R^i}+\frac{\partial^2 w_0^i}{\partial R^{i2}}\right)\right]\\+\left[A_{12}^i\frac{u_0^i}{R^i}+B_{12}^i\frac{u_1}{R}-D_{12}^ic_1\left(\frac{u_1^i}{R^i}+\frac{\partial w_0^i}{R^i\partial R^i}\right)\right]-X_{31}\phi\end{array}\right)\\-\frac{1}{R}\left(\begin{array}{l}\left[A_{12}^i\frac{\partial u_0^i}{\partial R^i}+B_{12}^i\frac{\partial u_1^i}{\partial R^i}-D_{12}^ic_1\left(\frac{\partial u_1^i}{\partial R^i}+\frac{\partial^2 w_0^i}{\partial R^{i2}}\right)\right]\\+Q_{22}^i\left[A_{22}^i\frac{u_0^i}{R^i}+B_{22}^i\frac{u_1^i}{R^i}-D_{22}^ic_1\left(\frac{u_1^i}{R^i}+\frac{\partial w_0^i}{R^i\partial R^i}\right)\right]\end{array}\right)\end{array}\right]=0;\quad i=c,p \tag{P-1}$$

δw_0^i :

$$(1-l^2\nabla^2)\left[\begin{array}{l}c_1\frac{\partial^2}{\partial R^{i2}}\left(\begin{array}{l}\left[D_{11}^i\frac{\partial u_0^i}{\partial R^i}+E_{11}^i\frac{\partial u_1^i}{\partial R^i}-G_{11}^ic_1\left(\frac{\partial u_1^i}{\partial R^i}+\frac{\partial^2 w_0^i}{\partial R^{i2}}\right)\right]\\+\left[D_{12}^i\frac{u_0^i}{R^i}+E_{12}^i\frac{u_1^i}{R^i}-G_{12}^ic_1\left(\frac{u_1^i}{R^i}+\frac{\partial w_0^i}{R^i\partial R^i}\right)\right]-X_{33}\phi\end{array}\right)\\-c_1\frac{\partial}{R^i\partial R^i}\left(\begin{array}{l}\left[D_{12}^i\frac{\partial u_0^i}{\partial R^i}+E_{12}^i\frac{\partial u_1^i}{\partial R^i}-G_{12}^ic_1\left(\frac{\partial u_1^i}{\partial R^i}+\frac{\partial^2 w_0^i}{\partial R^{i2}}\right)\right]\\+Q_{22}^i\left[D_{22}^i\frac{u_0^i}{R^i}+E_{22}^i\frac{u_1^i}{R^i}-G_{22}^ic_1\left(\frac{u_1^i}{R^i}+\frac{\partial w_0^i}{R^i\partial R^i}\right)\right]\end{array}\right)\\+\frac{\partial}{\partial R^i}\left((A_{55}^i-3C_{55}^ic_1)\left(u_1^i+\frac{\partial w_0^i}{\partial R^i}\right)+X_{11}\partial\phi/\partial R\right)\\-3c_1\frac{\partial}{\partial R^i}\left((C_{55}^i-3E_{55}^ic_1)\left(u_1^i+\frac{\partial w_0^i}{\partial R^i}\right)+X_{12}\partial\phi/\partial R^i\right)-N_1^pw_{0,x^2}^i\end{array}\right]=0;\quad i=c,p \tag{P-2}$$

δu_1^i :

$$(1-l^2\nabla^2)\left[\begin{array}{l}\frac{\partial}{\partial R^i}\left(\begin{array}{l}\left[B_{11}^i\frac{\partial u_0^i}{\partial R^i}+C_{11}^i\frac{\partial u_1^i}{\partial R^i}-E_{11}^ic_1\left(\frac{\partial u_1^i}{\partial R^i}+\frac{\partial^2 w_0^i}{\partial R^{i2}}\right)\right]\\+\left[B_{12}^i\frac{u_0^i}{R^i}+C_{12}^i\frac{u_1^i}{R^i}-E_{12}^ic_1\left(\frac{u_1^i}{R^i}+\frac{\partial w_0^i}{R^i\partial R^i}\right)\right]-X_{32}\phi\end{array}\right)\\-\frac{c_1\partial}{\partial R^i}\left(\begin{array}{l}\left[D_{11}^i\frac{\partial u_0^i}{\partial R^i}+E_{11}^i\frac{\partial u_1^i}{\partial R^i}-G_{11}^ic_1\left(\frac{\partial u_1^i}{\partial R^i}+\frac{\partial^2 w_0^i}{\partial R^{i2}}\right)\right]\\+\left[D_{12}^i\frac{u_0^i}{R^i}+E_{12}^i\frac{u_1^i}{R^i}-G_{12}^ic_1\left(\frac{u_1^i}{R^i}+\frac{\partial w_0^i}{R^i\partial R^i}\right)\right]-X_{33}\phi\end{array}\right)\\-\frac{1}{R^i}\left(\begin{array}{l}\left[B_{12}^i\frac{\partial u_0^i}{\partial R^i}+C_{12}^i\frac{\partial u_1^i}{\partial R^i}-E_{12}^ic_1\left(\frac{\partial u_1^i}{\partial R^i}+\frac{\partial^2 w_0^i}{\partial R^{i2}}\right)\right]\\+Q_{22}^i\left[B_{22}^i\frac{u_0^i}{R^i}+C_{22}^i\frac{u_1^i}{R^i}-E_{22}^ic_1\left(\frac{u_1^i}{R^i}+\frac{\partial w_0^i}{R^i\partial R^i}\right)\right]\end{array}\right)\\+\frac{c_1}{R^i}\left(\begin{array}{l}\left[D_{12}^i\frac{\partial u_0^i}{\partial R^i}+E_{12}^i\frac{\partial u_1^i}{\partial R^i}-G_{12}^ic_1\left(\frac{\partial u_1^i}{\partial R^i}+\frac{\partial^2 w_0^i}{\partial R^{i2}}\right)\right]\\+Q_{22}^i\left[D_{22}^i\frac{u_0^i}{R^i}+E_{22}^i\frac{u_1^i}{R^i}-G_{22}^ic_1\left(\frac{u_1^i}{R^i}+\frac{\partial w_0^i}{R^i\partial R^i}\right)\right]\end{array}\right)\\-\left[(A_{55}^i-3C_{55}^ic_1)\left(u_1^i+\frac{\partial w_0^i}{\partial R^i}\right)+X_{11}\partial\phi/\partial R^i\right]\\+3c_1\left(S_{Rz}^i=(C_{55}^i-3E_{55}^ic_1)\left(u_1^i+\frac{\partial w_0^i}{\partial R^i}\right)+X_{12}\partial\phi/\partial R^i\right)\end{array}\right]=0;\quad i=c,p \tag{P-3}$$

$\delta\phi$:

$$(1-l^2\nabla^2)\left(\begin{array}{l}+X_{31}\frac{\partial u_0^p}{\partial R^p}+(X_{11}-3X_{12})\frac{\partial^2 w_0^p}{\partial R^{p2}}-X_{33}\frac{\partial^2 w_0^p}{\partial R^{p2}}\\-(-X_{11}+3X_{12})\frac{\partial u_1^p}{\partial R^p}+X_{32}\frac{\partial u_1^p}{\partial R^p}-X_{33}\frac{\partial u_1^p}{\partial R^p}\\-X_{41}\frac{\partial^2\phi}{\partial R^{p2}}+X_{42}\phi\end{array}\right)=0 \tag{P-4}$$

The GDQ form can be given as follows:

δu_0^i :

$$\left(1-l^2\left(\sum_{v=1}^{N_n} C^{(2)}_{n,v}+\sum_{v=1}^{N_n} C^{(1)}_{n,v}\frac{1}{R^i}\right)\right)\left[\begin{array}{l}\left(\begin{array}{l}\left[\begin{array}{l}A^i_{11}\sum\limits_{v=1}^{N_n} C^{(2)}_{n,v}u^i_0+B^i_{11}\sum\limits_{v=1}^{N_n} C^{(2)}_{n,v}u^i_1\\ \quad -D^i_{11}c_1\left(\sum\limits_{v=1}^{N_n} C^{(2)}_{n,v}u^i_1+\sum\limits_{v=1}^{N_n} C^{(2)}_{n,v}w^i_0\right)\end{array}\right]\\ +\left[\begin{array}{l}+B^i_{12}\sum\limits_{v=1}^{N_n} C^{(1)}_{n,v}\frac{u^i_1}{R^i_n}+A^i_{12}\sum\limits_{v=1}^{N_n} C^{(1)}_{n,v}\frac{u^i_0}{R^i_n}\\ \quad -D^i_{12}c_1\left(\sum\limits_{v=1}^{N_n} C^{(1)}_{n,v}\frac{u^i_1}{R^i}+\sum\limits_{v=1}^{N_n} C^{(2)}_{n,v}\frac{w^i_0}{R^i_n}\right)\end{array}\right]-X_{31}\sum\limits_{v=1}^{N_n} C^{(1)}_{n,v}\phi_n\end{array}\right)\\ -\frac{1}{R}\left(\begin{array}{l}\left[\begin{array}{l}A^i_{12}\sum\limits_{v=1}^{N_n} C^{(1)}_{n,v}\frac{u^i_0}{R^i_n}+B^i_{12}\sum\limits_{v=1}^{N_n} C^{(1)}_{n,v}\frac{u^i_1}{R^i_n}\\ \quad -D^i_{12}c_1\left(\sum\limits_{v=1}^{N_n} C^{(1)}_{n,v}\frac{u^i_1}{R^i_n}+\sum\limits_{v=1}^{N_n} C^{(2)}_{n,v}\frac{w^i_0}{R^i_n}\right)\end{array}\right]\\ +Q^i_{22}\left[\begin{array}{l}A^i_{22}\sum\limits_{v=1}^{N_n}\frac{u^i_0}{R^{2i}{}_n}+B^i_{22}\sum\limits_{v=1}^{N_n}\frac{u^i_1}{R^{2i}{}_n}\\ \quad -D^i_{22}c_1\left(\sum\limits_{v=1}^{N_n}\frac{u^i_1}{R^{2i}{}_n}+\sum\limits_{v=1}^{N_n} C^{(1)}_{n,v}\frac{w^i_0}{R^{2i}{}_n}\right)\end{array}\right]\end{array}\right)\end{array}\right]=0;\quad i=c,p \tag{P-5}$$

δw_0^i :

$$\left(1-l^2\left(\sum_{v=1}^{N_n} C^{(2)}_{n,v}+\sum_{v=1}^{N_n} C^{(1)}_{n,v}\frac{1}{R^i}\right)\right)\left[\begin{array}{l}c_1\left(\begin{array}{l}\left[\begin{array}{l}D^i_{11}\sum\limits_{v=1}^{N_n} C^{(3)}_{n,v}u^i_0+E^i_{11}\sum\limits_{v=1}^{N_n} C^{(3)}_{n,v}u^i_1\\ \quad -G^i_{11}c_1\left(\sum\limits_{v=1}^{N_n} C^{(3)}_{n,v}u^i_1+\sum\limits_{v=1}^{N_n} C^{(4)}_{n,v}w^i_0\right)\end{array}\right]\\ +\left[\begin{array}{l}D^i_{12}\sum\limits_{v=1}^{N_n} C^{(2)}_{n,v}\frac{u^i_0}{R^i_n}+E^i_{12}\sum\limits_{v=1}^{N_n} C^{(2)}_{n,v}\frac{u^i_1}{R^i_n}\\ \quad -G^i_{12}c_1\left(\sum\limits_{v=1}^{N_n} C^{(2)}_{n,v}\frac{u^i_1}{R^i_n}+\sum\limits_{v=1}^{N_n} C^{(3)}_{n,v}\frac{w^i_0}{R^i_n}\right)\end{array}\right]-X_{33}\sum\limits_{v=1}^{N_n} C^{(2)}_{n,v}\phi\end{array}\right)\\ -c_1\left(\begin{array}{l}\left[\begin{array}{l}D^i_{12}\sum\limits_{v=1}^{N_n} C^{(2)}_{n,v}\frac{u^i_0}{R^i_n}+E^i_{12}\sum\limits_{v=1}^{N_n} C^{(2)}_{n,v}\frac{u^i_1}{R^i_n}\\ \quad -G^i_{12}c_1\left(\sum\limits_{v=1}^{N_n} C^{(2)}_{n,v}\frac{u^i_1}{R^i_n}+\sum\limits_{v=1}^{N_n} C^{(3)}_{n,v}\frac{w^i_0}{R^i_n}\right)\end{array}\right]\\ +Q^i_{22}\left[\begin{array}{l}D^i_{22}\sum\limits_{v=1}^{N_n} C^{(1)}_{n,v}\frac{u^i_0}{R^{2i}{}_n}+E^i_{22}\sum\limits_{v=1}^{N_n} C^{(1)}_{n,v}\frac{u^i_1}{R^{2i}{}_n}\\ \quad -G^i_{22}c_1\left(\sum\limits_{v=1}^{N_n} C^{(1)}_{n,v}\frac{u^i_1}{R^{2i}{}_n}+\sum\limits_{v=1}^{N_n} C^{(2)}_{n,v}\frac{w^i_0}{R^{2i}{}_n}\right)\end{array}\right]\end{array}\right)\\ +\left((A^i_{55}-3C^i_{55}c_1)\left(\sum\limits_{v=1}^{N_n} C^{(1)}_{n,v}u^i_1+\sum\limits_{v=1}^{N_n} C^{(2)}_{n,v}w^i_0\right)+X_{11}\sum\limits_{v=1}^{N_n} C^{(2)}_{n,v}\phi\right)\\ -3c_1\left(\begin{array}{l}(C^i_{55}-3E^i_{55}c_1)\left(\sum\limits_{v=1}^{N_n} C^{(1)}_{n,v}u^i_1+\sum\limits_{v=1}^{N_n} C^{(1)}_{n,v}w^i_0\right)\\ \quad +X_{12}\sum\limits_{v=1}^{N_n} C^{(2)}_{n,v}\phi\end{array}\right)-N^p_1\sum\limits_{v=1}^{N_n} C^{(2)}_{n,v}w^i_0\end{array}\right]=0;\quad i=c,p \tag{P-6}$$

δu_1^i :

$$
\left(1-l^2\left(\sum_{v=1}^{N_n} C_{n,v}^{(2)}+\sum_{v=1}^{N_n} C_{n,v}^{(1)}\frac{1}{R^i}\right)\right)
\left[
\begin{array}{l}
\left(\left[B_{11}^i\sum_{v=1}^{N_n}C_{n,v}^{(2)}u_0^i+C_{11}^i\sum_{v=1}^{N_n}C_{n,v}^{(2)}u_1^i-E_{11}^i c_1\left(\sum_{v=1}^{N_n}C_{n,v}^{(2)}u_1^i+\sum_{v=1}^{N_n}C_{n,v}^{(3)}w_0^i\right)\right]\right. \\
\left.+\left[B_{12}^i\sum_{v=1}^{N_n}C_{n,v}^{(1)}\frac{u_0^i}{R_n^i}+C_{12}^i\sum_{v=1}^{N_n}C_{n,v}^{(1)}\frac{u_1^i}{R_n^i}-E_{12}^i c_1\left(\sum_{v=1}^{N_n}C_{n,v}^{(1)}\frac{u_1^i}{R_n^i}+\sum_{v=1}^{N_n}C_{n,v}^{(2)}\frac{w_0^i}{R_n^i}\right)\right]-X_{32}\sum_{v=1}^{N_n}C_{n,v}^{(1)}\phi\right) \\
-c_1\left(\left[D_{11}^i\sum_{v=1}^{N_n}C_{n,v}^{(2)}u_0^i+E_{11}^i\sum_{v=1}^{N_n}C_{n,v}^{(2)}u_1^i-G_{11}^i c_1\left(\sum_{v=1}^{N_n}C_{n,v}^{(2)}u_1^i+\sum_{v=1}^{N_n}C_{n,v}^{(3)}w_0^i\right)\right]\right. \\
\left.+\left[D_{12}^i\sum_{v=1}^{N_n}C_{n,v}^{(1)}\frac{u_0^i}{R_n^i}+E_{12}^i\sum_{v=1}^{N_n}C_{n,v}^{(1)}\frac{u_1^i}{R_n^i}-G_{12}^i c_1\left(\sum_{v=1}^{N_n}C_{n,v}^{(1)}\frac{u_1^i}{R_n^i}+\sum_{v=1}^{N_n}C_{n,v}^{(2)}\frac{w_0^i}{R_n^i}\right)\right]-X_{33}\sum_{v=1}^{N_n}C_{n,v}^{(1)}\phi\right) \\
-\left(\left[B_{12}^i\sum_{v=1}^{N_n}C_{n,v}^{(1)}\frac{u_0^i}{R_n^i}+C_{12}^i\sum_{v=1}^{N_n}C_{n,v}^{(1)}\frac{u_1^i}{R_n^i}-E_{12}^i c_1\left(\sum_{v=1}^{N_n}C_{n,v}^{(1)}\frac{u_1^i}{R_n^i}+\sum_{v=1}^{N_n}C_{n,v}^{(2)}\frac{w_0^i}{R_n^i}\right)\right]\right. \\
\left.+Q_{22}^i\left[B_{22}^i\sum_{v=1}^{N_n}\frac{u_0^i}{R^{2i}{}_n}+C_{22}^i\sum_{v=1}^{N_n}\frac{u_1^i}{R^{2i}{}_n}-E_{22}^i c_1\left(\sum_{v=1}^{N_n}\frac{u_1^i}{R^{2i}{}_n}+\sum_{v=1}^{N_n}C_{n,v}^{(1)}\frac{w_0^i}{R^{2i}{}_n}\right)\right]\right) \\
+c_1\left(\left[D_{12}^i\sum_{v=1}^{N_n}C_{n,v}^{(1)}\frac{u_0^i}{R_n^i}+E_{12}^i\sum_{v=1}^{N_n}C_{n,v}^{(1)}\frac{u_1^i}{R_n^i}-G_{12}^i c_1\left(\sum_{v=1}^{N_n}C_{n,v}^{(1)}\frac{u_1^i}{R_n^i}+\sum_{v=1}^{N_n}C_{n,v}^{(2)}\frac{w_1^i}{R_n^i}\right)\right]\right. \\
\left.+Q_{22}^i\left[D_{22}^i\sum_{v=1}^{N_n}\frac{u_0^i}{R^{2i}{}_n}+E_{22}^i\sum_{v=1}^{N_n}\frac{u_1^i}{R^{2i}{}_n}-G_{22}^i c_1\left(\sum_{v=1}^{N_n}\frac{u_1^i}{R^{2i}{}_n}+\sum_{v=1}^{N_n}C_{n,v}^{(1)}\frac{w_0^i}{R^{2i}{}_n}\right)\right]\right) \\
-\left[(A_{55}^i-3C_{55}^i c_1)\left(\sum_{v=1}^{N_n}u_0^i I_v+\sum_{v=1}^{N_n}C_{n,v}^{(1)}w_0^i\right)+X_{11}\sum_{v=1}^{N_n}C_{n,v}^{(1)}\phi\right] \\
+3c_1\left((C_{55}^i-3E_{55}^i c_1)\left(\sum_{v=1}^{N_n}u_1^i I_v+\sum_{v=1}^{N_n}C_{n,v}^{(1)}w_0^i\right)+X_{12}\sum_{v=1}^{N_n}C_{n,v}^{(1)}\phi\right)
\end{array}
\right]=0;\quad i=c,p \tag{P-7}
$$

$\delta\phi$:

$$
\left(1-l^2\left(\sum_{v=1}^{N_n} C_{n,v}^{(2)}+\sum_{v=1}^{N_n} C_{n,v}^{(1)}\frac{1}{R^i}\right)\right)
\left(
\begin{array}{l}
+X_{31}\sum_{v=1}^{N_n}C_{n,v}^{(1)}u_0^p+(X_{11}-3X_{12}-X_{33})\sum_{v=1}^{N_n}C_{n,v}^{(2)}w_0^p \\
-(-X_{11}+3X_{12}-X_{32}+X_{33})\sum_{v=1}^{N_n}C_{n,v}^{(1)}u_1^p \\
-X_{41}\sum_{v=1}^{N_n}C_{n,v}^{(2)}\phi+X_{42}\sum_{v=1}^{N_n}\phi I_v
\end{array}
\right)=0 \tag{P-8}
$$

References

1. Safarpour M, Ghabussi A, Ebrahimi F, Habibi M, Safarpour H (2020) Frequency characteristics of FG-GPLRC viscoelastic thick annular plate with the aid of GDQM. Thin Walled Struct 150:106683
2. Safarpour M, Ebrahimi F, Habibi M, Safarpour H (2020) On the nonlinear dynamics of a multi-scale hybrid nanocomposite disk. Eng Comput. https://doi.org/10.1007/s00366-020-00949-5
3. Moayedi H, Habibi M, Safarpour H, Safarpour M, Foong L (2020) Buckling and frequency responses of a graphene nanoplatelet reinforced composite microdisk. Int J Appl Mech. https://doi.org/10.1142/S1758825119501023
4. Safarpour M, Rahimi A, Alibeigloo A (2019) Static and free vibration analysis of graphene platelets reinforced composite truncated conical shell, cylindrical shell, and annular plate using theory of elasticity and DQM. Mech Based Des Struct Mach. https://doi.org/10.1080/15397734.2019.1646137
5. Shahgholian-Ghahfarokhi D, Safarpour M, Rahimi A (2019) Torsional buckling analyses of functionally graded porous nanocomposite cylindrical shells reinforced with graphene platelets (GPLs). Mech Based Des Struct Mach. https://doi.org/10.1080/15397734.2019.1666723
6. Bisheh H, Alibeigloo A, Safarpour M, Rahimi A (2019) Three-dimensional static and free vibrational analysis of graphene reinforced composite circular/annular plate using differential quadrature method. Int J Appl Mech 11:1950073
7. Safarpour M, Rahimi A, Alibeigloo A, Bisheh H, Forooghi A (2019) Parametric study of three-dimensional bending and frequency of FG-GPLRC porous circular and annular plates on different boundary conditions. Mech Based Des Struct Mach. https://doi.org/10.1080/15397734.2019.1701491
8. Rahimi A, Alibeigloo A, Safarpour M (2020) Three-dimensional static and free vibration analysis of graphene platelet–reinforced porous composite cylindrical shell. J Vib Control. https://doi.org/10.1177/1077546320902340
9. Wang Y, Zeng R, Safarpour M (2020) Vibration analysis of FG-GPLRC annular plate in a thermal environment. Mech Based Des Struct Mach 1–19
10. Shahgholian D, Safarpour M, Rahimi A, Alibeigloo A (2020) Buckling analyses of functionally graded graphene-reinforced porous cylindrical shell using the Rayleigh–Ritz method. Acta Mech 1–16
11. Qiao W, Yang Z, Kang Z, Pan Z (2020) Short-term natural gas consumption prediction based on Volterra adaptive filter and improved whale optimization algorithm. Eng Appl Artif Intell 87:103323
12. Qiao W, Yang Z (2019) Forecast the electricity price of US using a wavelet transform-based hybrid model. Energy 163:116704. https://doi.org/10.1016/j.energy.2019.116704
13. Qiao W, Yang Z (2019) Solving large-scale function optimization problem by using a new metaheuristic algorithm based on quantum dolphin swarm algorithm. IEEE Access 7:138972–138989
14. Qiao W, Tian W, Tian Y, Yang Q, Wang Y, Zhang J (2019) The forecasting of PM2. 5 using a hybrid model based on wavelet transform and an improved deep learning algorithm. IEEE Access 7:142814–142825
15. Qiao W, Yang Z (2019) Modified dolphin swarm algorithm based on chaotic maps for solving high-dimensional function optimization problems. IEEE Access 7:110472–110486
16. Qiao W, Huang K, Azimi M, Han S (2019) A novel hybrid prediction model for hourly gas consumption in supply side based on improved machine learning algorithms. IEEE Access 7:88218–88230. https://doi.org/10.1109/ACCESS.2019.2918156
17. Derazkola HA, Eyvazian A, Simchi A (2020) Modeling and experimental validation of material flow during FSW of polycarbonate. Mater Today Commun 22:100796
18. Eyvazian A, Hamouda A, Tarlochan F, Derazkola HA, Khodabakhshi F (2020) Simulation and experimental study of underwater dissimilar friction-stir welding between aluminium and steel. J Mater Res Technol. https://doi.org/10.1016/j.jmrt.2020.02.003
19. Eyvazian A, Hamouda AM, Aghajani Derazkola H, Elyasi M (2020) Study on the effects of tool tile angle, offset and plunge depth on friction stir welding of poly (methyl methacrylate) T-joint. Proc Inst Mech Eng Part B J Eng Manuf 234:773–787
20. Derazkola HA, Eyvazian A, Simchi A (2020) Submerged friction stir welding of dissimilar joints between an Al–Mg alloy and low carbon steel: thermo-mechanical modeling, microstructural features, and mechanical properties. J Manuf Process 50:68–79
21. Nadri S, Xie L, Jafari M, Alijabbari N, Cyberey ME, Barker NS et al (2018) A 160 GHz frequency quadrupler based on heterogeneous integration of GaAs Schottky diodes onto silicon using SU-8 for epitaxy transfer. In: 2018 IEEE/MTT-S international microwave symposium-IMS, 2018, pp 769–772
22. Jafari M, Moradi G, Shirazi RS, Mirzavand R (2017) Design and implementation of a six-port junction based on substrate integrated waveguide. Turk J Electr Eng Comput Sci 25:2547–2553
23. Alkhatib SE, Tarlochan F, Eyvazian A (2017) Collapse behavior of thin-walled corrugated tapered tubes. Eng Struct 150:674–692
24. Hedayati R, Ziaei-Rad S, Eyvazian A, Hamouda AM (2014) Bird strike analysis on a typical helicopter windshield with different lay-ups. J Mech Sci Technol 28:1381–1392
25. Mozafari H, Eyvazian A, Hamouda AM, Crupi V, Epasto G, Gugliemino E (2018) Numerical and experimental investigation of corrugated tubes under lateral compression. Int J Crashworthiness 23:461–473
26. Eyvazian A, Akbarzadeh I, Shakeri M (2012) Experimental study of corrugated tubes under lateral loading. Proc Inst Mech Eng Part L J Mater Des Appl 226:109–118
27. Eyvazian A, Habibi MK, Hamouda AM, Hedayati R (2014) Axial crushing behavior and energy absorption efficiency of corrugated tubes. Mater Des 1980–2015(54):1028–1038
28. Eyvazian A, Tran T, Hamouda AM (2018) Experimental and theoretical studies on axially crushed corrugated metal tubes. Int J Non Linear Mech 101:86–94
29. Dastjerdi AA, Shahsavari H, Eyvazian A, Tarlochan F (2019) Crushing analysis and multi-objective optimization of different length bi-thin walled cylindrical structures under axial impact loading. Eng Optim 51:1884–1901
30. Sadighi A, Eyvazian A, Asgari M, Hamouda AM (2019) A novel axially half corrugated thin-walled tube for energy absorption under axial loading. Thin Walled Struct 145:106418
31. Eyvazian A, Taghizadeh SA, Hamouda AM, Tarlochan F, Moeinifard M, Gobbi M (2019) Buckling and crushing behavior of foam-core hybrid composite sandwich columns under quasi-static edgewise compression. J Sandw Struct Mater. https://doi.org/10.1177/1099636219894665
32. Sun J, Zhao J (2018) Multi-layer graphene reinforced nano-laminated WC-Co composites. Mater Sci Eng A 723:1–7
33. Rafiee MA, Rafiee J, Wang Z, Song H, Yu Z-Z, Koratkar N (2009) Enhanced mechanical properties of nanocomposites at low graphene content. ACS Nano 3:3884–3890
34. Zhong R, Wang Q, Tang J, Shuai C, Qin B (2018) Vibration analysis of functionally graded carbon nanotube reinforced composites (FG-CNTRC) circular, annular and sector plates. Compos Struct 194:49–67
35. Yang Y, Wang Z, Wang Y (2018) Thermoelastic coupling vibration and stability analysis of rotating circular plate in friction clutch. J Low Freq Noise Vib Active Control 38:558–573. https://doi.org/10.1177/1461348418817465

36. Ghabussi A, Ashrafi N, Shavalipour A, Hosseinpour A, Habibi M, Moayedi H et al (2019) Free vibration analysis of an electro-elastic GPLRC cylindrical shell surrounded by viscoelastic foundation using modified length-couple stress parameter. Mech Based Des Struct Mach. https://doi.org/10.1080/15397734.2019.1705166
37. Habibi M, Mohammadi A, Safarpour H, Ghadiri M (2019) Effect of porosity on buckling and vibrational characteristics of the imperfect GPLRC composite nanoshell. Mech Based Des Struct Mach. https://doi.org/10.1080/15397734.2019.1701490
38. Habibi M, Mohammadi A, Safarpour H, Shavalipour A, Ghadiri M (2019) Wave propagation analysis of the laminated cylindrical nanoshell coupled with a piezoelectric actuator. Mech Based Des Struct Mach. https://doi.org/10.1080/15397734.2019.1697932
39. Ebrahimi F, Mohammadi K, Barouti MM, Habibi M (2019) Wave propagation analysis of a spinning porous graphene nanoplatelet-reinforced nanoshell. Waves Random Complex Media. https://doi.org/10.1080/17455030.2019.1694729
40. Shokrgozar A, Safarpour H, Habibi M (2019) Influence of system parameters on buckling and frequency analysis of a spinning cantilever cylindrical 3D shell coupled with piezoelectric actuator. Proc Inst Mech Eng Part C J Mech Eng Sci 234(2):512–529. https://doi.org/10.1177/0954406219883312
41. Habibi M, Taghdir A, Safarpour H (2019) Stability analysis of an electrically cylindrical nanoshell reinforced with graphene nanoplatelets. Compos B Eng 175:107125
42. Mohammadgholiha M, Shokrgozar A, Habibi M, Safarpour H (2019) Buckling and frequency analysis of the nonlocal strain–stress gradient shell reinforced with graphene nanoplatelets. J Vib Control 25:2627–2640
43. Ebrahimi F, Habibi M, Safarpour H (2019) On modeling of wave propagation in a thermally affected GNP-reinforced imperfect nanocomposite shell. Eng Comput 35:1375–1389
44. Safarpour H, Hajilak ZE, Habibi M (2019) A size-dependent exact theory for thermal buckling, free and forced vibration analysis of temperature dependent FG multilayer GPLRC composite nanostructures restring on elastic foundation. Int J Mech Mater Des 15:569–583
45. Hashemi HR, Alizadeh AA, Oyarhossein MA, Shavalipour A, Makkiabadi M, Habibi M (2019) Influence of imperfection on amplitude and resonance frequency of a reinforcement compositionally graded nanostructure. Waves Random Complex Media. https://doi.org/10.1080/17455030.2019.1662968
46. Ebrahimi F, Hashemabadi D, Habibi M, Safarpour H (2019) Thermal buckling and forced vibration characteristics of a porous GNP reinforced nanocomposite cylindrical shell. Microsyst Technol 26:1–13. https://doi.org/10.1007/s00542-019-04542-9
47. Mohammadi A, Lashini H, Habibi M, Safarpour H (2019) Influence of viscoelastic foundation on dynamic behaviour of the double walled cylindrical inhomogeneous micro shell using MCST and with the aid of GDQM. J Solid Mech 11:440–453
48. Habibi M, Hashemabadi D, Safarpour H (2019) Vibration analysis of a high-speed rotating GPLRC nanostructure coupled with a piezoelectric actuator. Eur Phys J Plus 134:307
49. Pourjabari A, Hajilak ZE, Mohammadi A, Habibi M, Safarpour H (2019) Effect of porosity on free and forced vibration characteristics of the GPL reinforcement composite nanostructures. Comput Math Appl 77:2608–2626
50. Habibi M, Mohammadgholiha M, Safarpour H (2019) Wave propagation characteristics of the electrically GNP-reinforced nanocomposite cylindrical shell. J Braz Soc Mech Sci Eng 41:221
51. Safarpour H, Pourghader J, Habibi M (2019) Influence of spring-mass systems on frequency behavior and critical voltage of a high-speed rotating cantilever cylindrical three-dimensional shell coupled with piezoelectric actuator. J Vib Control 25:1543–1557
52. Ebrahimi F, Hajilak ZE, Habibi M, Safarpour H (2019) Buckling and vibration characteristics of a carbon nanotube-reinforced spinning cantilever cylindrical 3D shell conveying viscous fluid flow and carrying spring-mass systems under various temperature distributions. Proc Inst Mech Eng Part C J Mech Eng Sci 233:4590–4605
53. Esmailpoor Hajilak Z, Pourghader J, Hashemabadi D, Sharifi Bagh F, Habibi M, Safarpour H (2019) Multilayer GPLRC composite cylindrical nanoshell using modified strain gradient theory. Mech Based Des Struct Mach 45:521–545
54. Safarpour H, Ghanizadeh SA, Habibi M (2018) Wave propagation characteristics of a cylindrical laminated composite nanoshell in thermal environment based on the nonlocal strain gradient theory. Eur Phys J Plus 133:532
55. Gao W, Dimitrov D, Abdo H (2018) Tight independent set neighborhood union condition for fractional critical deleted graphs and ID deleted graphs. Discrete Contin Dyn Syst S 12:711–721
56. Gao W, Guirao JLG, Basavanagoud B, Wu J (2018) Partial multi-dividing ontology learning algorithm. Inf Sci 467:35–58
57. Gao W, Wang W, Dimitrov D, Wang Y (2018) Nano properties analysis via fourth multiplicative ABC indicator calculating. Arab J Chem 11:793–801
58. Gao W, Wu H, Siddiqui MK, Baig AQ (2018) Study of biological networks using graph theory. Saudi J Biol Sci 25:1212–1219
59. Gao W, Guirao JLG, Abdel-Aty M, Xi W (2019) An independent set degree condition for fractional critical deleted graphs. Discrete Contin Dyn Syst S 12:877–886
60. Medani M, Benahmed A, Zidour M, Heireche H, Tounsi A, Bousahla AA et al (2019) Static and dynamic behavior of (FG-CNT) reinforced porous sandwich plate using energy principle. Steel Compos Struct 32:595–610
61. Karami B, Shahsavari D, Janghorban M, Tounsi A (2019) Resonance behavior of functionally graded polymer composite nanoplates reinforced with graphene nanoplatelets. Int J Mech Sci 156:94–105
62. Draoui A, Zidour M, Tounsi A, Adim B (2019) Static and dynamic behavior of nanotubes-reinforced sandwich plates using (FSDT). J Nano Res 57:117–135. https://doi.org/10.4028/www.scientific.net/JNanoR.57.117
63. Bakhadda B, Bouiadjra MB, Bourada F, Bousahla AA, Tounsi A, Mahmoud S (2018) Dynamic and bending analysis of carbon nanotube-reinforced composite plates with elastic foundation. Wind Struct 27:311–324
64. Eyvazian A, Hamouda AM, Tarlochan F, Mohsenizadeh S, Dastjerdi AA (2019) Damping and vibration response of viscoelastic smart sandwich plate reinforced with non-uniform graphene platelet with magnetorheological fluid core. Steel Compos Struct 33:891
65. Motezaker M, Eyvazian A (2020) Post-buckling analysis of Mindlin cut out-plate reinforced by FG-CNTs. Steel Compos Struct 34:289
66. Alipour M (2018) Transient forced vibration response analysis of heterogeneous sandwich circular plates under viscoelastic boundary support. Arch Civ Mech Eng 18:12–31
67. Ebrahimi F, Rastgo A (2008) An analytical study on the free vibration of smart circular thin FGM plate based on classical plate theory. Thin Walled Struct 46:1402–1408
68. Ebrahimi F, Rastgoo A (2008) Free vibration analysis of smart annular FGM plates integrated with piezoelectric layers. Smart Mater Struct 17:015044
69. Zhou S, Zhang R, Zhou S, Li A (2019) Free vibration analysis of bilayered circular micro-plate including surface effects. Appl Math Model 70:54–66
70. Mohammadimehr M, Emdadi M, Afshari H, Rousta Navi B (2018) Bending, buckling and vibration analyses of MSGT microcomposite circular-annular sandwich plate under

hydro-thermo-magneto-mechanical loadings using DQM. Int J Smart Nano Mater 9:233–260
71. Mohammadimehr M, Atifeh SJ, Rousta Navi B (2018) Stress and free vibration analysis of piezoelectric hollow circular FG-SWBNNTs reinforced nanocomposite plate based on modified couple stress theory subjected to thermo-mechanical loadings. J Vib Control 24:3471–3486
72. Sajadi B, Alijani F, Goosen H, van Keulen F (2018) Effect of pressure on nonlinear dynamics and instability of electrically actuated circular micro-plates. Nonlinear Dyn 91:2157–2170
73. Wang Z-W, Han Q-F, Nash DH, Liu P-Q (2017) Investigation on inconsistency of theoretical solution of thermal buckling critical temperature rise for cylindrical shell. Thin Walled Struct 119:438–446
74. Shokrgozar A, Ghabussi A, Ebrahimi F, Habibi M, Safarpour H (2020) Viscoelastic dynamics and static responses of a graphene nanoplatelets-reinforced composite cylindrical microshell. Mech Based Des Struct Mach. https://doi.org/10.1080/15397734.2020.1719509
75. Ebrahimi F, Supeni EEB, Habibi M, Safarpour H (2020) Frequency characteristics of a GPL-reinforced composite microdisk coupled with a piezoelectric layer. Eur Phys J Plus 135:144
76. Moayedi H, Aliakbarlou H, Jebeli M, Noormohammadi Arani O, Habibi M, Safarpour H et al (2019) Thermal buckling responses of a graphene reinforced composite micropanel structure. Int J Appl Mech. https://doi.org/10.1142/S1758825120500106
77. Esmailpoor Hajilak Z, Pourghader J, Hashemabadi D, Sharifi Bagh F, Habibi M, Safarpour H (2019) Multilayer GPLRC composite cylindrical nanoshell using modified strain gradient theory. Mech Based Des Struct Mach 47:521–545
78. Karami B, Janghorban M, Tounsi A (2019) Galerkin's approach for buckling analysis of functionally graded anisotropic nanoplates/different boundary conditions. Eng Comput 35:1297–1316
79. Alimirzaei S, Mohammadimehr M, Tounsi A (2019) Nonlinear analysis of viscoelastic micro-composite beam with geometrical imperfection using FEM: MSGT electro-magneto-elastic bending, buckling and vibration solutions. Struct Eng Mech 71:485–502
80. Karami B, Janghorban M, Tounsi A (2019) Wave propagation of functionally graded anisotropic nanoplates resting on Winkler–Pasternak foundation. Struct Eng Mech 70:55–66
81. Karami B, Janghorban M, Tounsi A (2019) On exact wave propagation analysis of triclinic material using three-dimensional bi-Helmholtz gradient plate model. Struct Eng Mech 69:487–497
82. Karami B, Janghorban M, Shahsavari D, Tounsi A (2018) A size-dependent quasi-3D model for wave dispersion analysis of FG nanoplates. Steel Compos Struct 28:99–110
83. Karami B, Janghorban M, Tounsi A (2018) Nonlocal strain gradient 3D elasticity theory for anisotropic spherical nanoparticles. Steel Compos Struct 27:201–216
84. Karami B, Janghorban M, Tounsi A (2018) Variational approach for wave dispersion in anisotropic doubly-curved nanoshells based on a new nonlocal strain gradient higher order shell theory. Thin Walled Struct 129:251–264
85. Karami B, Janghorban M, Tounsi A (2017) Effects of triaxial magnetic field on the anisotropic nanoplates. Steel Compos Struct 25:361–374
86. Wang K, Wang B, Zhang C (2017) Surface energy and thermal stress effect on nonlinear vibration of electrostatically actuated circular micro-/nanoplates based on modified couple stress theory. Acta Mech 228:129–140
87. Mahinzare M, Alipour MJ, Sadatsakkak SA, Ghadiri M (2019) A nonlocal strain gradient theory for dynamic modeling of a rotary thermo piezo electrically actuated nano FG circular plate. Mech Syst Signal Process 115:323–337
88. Mahinzare M, Ranjbarpur H, Ghadiri M (2018) Free vibration analysis of a rotary smart two directional functionally graded piezoelectric material in axial symmetry circular nanoplate. Mech Syst Signal Process 100:188–207
89. Berghouti H, Adda Bedia E, Benkhedda A, Tounsi A (2019) Vibration analysis of nonlocal porous nanobeams made of functionally graded material. Adv Nano Res 7:351–364
90. Boutaleb S, Benrahou KH, Bakora A, Algarni A, Bousahla AA, Tounsi A et al (2019) Dynamic analysis of nanosize FG rectangular plates based on simple nonlocal quasi 3D HSDT. Adv Nano Res 7:191
91. Hamza-Cherif R, Meradjah M, Zidour M, Tounsi A, Belmahi S, Bensattalah T (2018) Vibration analysis of nano beam using differential transform method including thermal effect. J Nano Res 54:1–14. https://doi.org/10.4028/www.scientific.net/JNanoR.54.1
92. Youcef DO, Kaci A, Benzair A, Bousahla AA, Tounsi A (2018) Dynamic analysis of nanoscale beams including surface stress effects. Smart Struct Syst 21:65–74
93. Bouadi A, Bousahla AA, Houari MSA, Heireche H, Tounsi A (2018) A new nonlocal HSDT for analysis of stability of single layer graphene sheet. Adv Nano Res 6:147
94. Bellifa H, Benrahou KH, Bousahla AA, Tounsi A, Mahmoud S (2017) A nonlocal zeroth-order shear deformation theory for nonlinear postbuckling of nanobeams. Struct Eng Mech 62:695–702
95. Bounouara F, Benrahou KH, Belkorissat I, Tounsi A (2016) A nonlocal zeroth-order shear deformation theory for free vibration of functionally graded nanoscale plates resting on elastic foundation. Steel Compos Struct 20:227–249
96. Al-Basyouni K, Tounsi A, Mahmoud S (2015) Size dependent bending and vibration analysis of functionally graded micro beams based on modified couple stress theory and neutral surface position. Compos Struct 125:621–630
97. Song M, Kitipornchai S, Yang J (2017) Free and forced vibrations of functionally graded polymer composite plates reinforced with graphene nanoplatelets. Compos Struct 159:579–588
98. De Villoria RG, Miravete A (2007) Mechanical model to evaluate the effect of the dispersion in nanocomposites. Acta Mater 55:3025–3031
99. Liu W, Zhang Z, Chen J, Jiang D, Fei W, Fan J, Li Y (2020) Feasibility evaluation of large-scale underground hydrogen storage in bedded salt rocks of China: a case study in Jiangsu province. Energy 9:117348. https://doi.org/10.1016/j.energy.2020.117348
100. Bouhadra A, Tounsi A, Bousahla AA, Benyoucef S, Mahmoud S (2018) Improved HSDT accounting for effect of thickness stretching in advanced composite plates. Struct Eng Mech 66:61–73
101. Zarga D, Tounsi A, Bousahla AA, Bourada F, Mahmoud S (2019) Thermomechanical bending study for functionally graded sandwich plates using a simple quasi-3D shear deformation theory. Steel Compos Struct 32:389–410
102. Boukhlif Z, Bouremana M, Bourada F, Bousahla AA, Bourada M, Tounsi A et al (2019) A simple quasi-3D HSDT for the dynamics analysis of FG thick plate on elastic foundation. Steel Compos Struct 31:503–516
103. Boulefrakh L, Hebali H, Chikh A, Bousahla AA, Tounsi A, Mahmoud S (2019) The effect of parameters of visco-Pasternak foundation on the bending and vibration properties of a thick FG plate. Geomech Eng 18:161–178
104. Mahmoudi A, Benyoucef S, Tounsi A, Benachour A, Adda Bedia EA, Mahmoud S (2019) A refined quasi-3D shear deformation theory for thermo-mechanical behavior of functionally graded sandwich plates on elastic foundations. J Sandw Struct Mater 21:1906–1929

105. Zaoui FZ, Ouinas D, Tounsi A (2019) New 2D and quasi-3D shear deformation theories for free vibration of functionally graded plates on elastic foundations. Compos B Eng 159:231–247
106. Younsi A, Tounsi A, Zaoui FZ, Bousahla AA, Mahmoud S (2018) Novel quasi-3D and 2D shear deformation theories for bending and free vibration analysis of FGM plates. Geomech Eng 14:519–532
107. Benchohra M, Driz H, Bakora A, Tounsi A, Adda Bedia E, Mahmoud S (2018) A new quasi-3D sinusoidal shear deformation theory for functionally graded plates. Struct Eng Mech 65:19–31
108. Abualnour M, Houari MSA, Tounsi A, Mahmoud S (2018) A novel quasi-3D trigonometric plate theory for free vibration analysis of advanced composite plates. Compos Struct 184:688–697
109. Atmane HA, Tounsi A, Bernard F (2017) Effect of thickness stretching and porosity on mechanical response of a functionally graded beams resting on elastic foundations. Int J Mech Mater Des 13:71–84
110. Draiche K, Tounsi A, Mahmoud S (2016) A refined theory with stretching effect for the flexure analysis of laminated composite plates. Geomech Eng 11:671–690
111. Bousahla AA, Houari MSA, Tounsi A, Adda Bedia EA (2014) A novel higher order shear and normal deformation theory based on neutral surface position for bending analysis of advanced composite plates. Int J Comput Methods 11:1350082
112. Chaabane LA, Bourada F, Sekkal M, Zerouati S, Zaoui FZ, Tounsi A et al (2019) Analytical study of bending and free vibration responses of functionally graded beams resting on elastic foundation. Struct Eng Mech 71:185–196
113. Bourada F, Bousahla AA, Bourada M, Azzaz A, Zinata A, Tounsi A (2019) Dynamic investigation of porous functionally graded beam using a sinusoidal shear deformation theory. Wind Struct 28:19–30
114. Liu W, Zhang X, Fan J, Li Y, Wang L (2020) Evaluation of potential for salt cavern gas storage and integration of brine extraction: cavern utilization, Yangtze River Delta region. Nat Resour Res. https://doi.org/10.1007/s11053-020-09640-4
115. Meksi R, Benyoucef S, Mahmoudi A, Tounsi A, Adda Bedia EA, Mahmoud S (2019) An analytical solution for bending, buckling and vibration responses of FGM sandwich plates. J Sandw Struct Mater 21:727–757
116. Bourada F, Amara K, Bousahla AA, Tounsi A, Mahmoud S (2018) A novel refined plate theory for stability analysis of hybrid and symmetric S-FGM plates. Struct Eng Mech 68:661–675
117. Zine A, Tounsi A, Draiche K, Sekkal M, Mahmoud S (2018) A novel higher-order shear deformation theory for bending and free vibration analysis of isotropic and multilayered plates and shells. Steel Compos Struct 26:125–137
118. Fourn H, Atmane HA, Bourada M, Bousahla AA, Tounsi A, Mahmoud S (2018) A novel four variable refined plate theory for wave propagation in functionally graded material plates. Steel Compos Struct 27:109–122
119. Attia A, Bousahla AA, Tounsi A, Mahmoud S, Alwabli AS (2018) A refined four variable plate theory for thermoelastic analysis of FGM plates resting on variable elastic foundations. Struct Eng Mech 65:453–464
120. Chikh A, Tounsi A, Hebali H, Mahmoud S (2017) Thermal buckling analysis of cross-ply laminated plates using a simplified HSDT. Smart Struct Syst 19:289–297
121. Menasria A, Bouhadra A, Tounsi A, Bousahla AA, Mahmoud S (2017) A new and simple HSDT for thermal stability analysis of FG sandwich plates. Steel Compos Struct 25:157–175
122. El-Haina F, Bakora A, Bousahla AA, Tounsi A, Mahmoud S (2017) A simple analytical approach for thermal buckling of thick functionally graded sandwich plates. Struct Eng Mech 63:585–595
123. Abdelaziz HH, Meziane MAA, Bousahla AA, Tounsi A, Mahmoud S, Alwabli AS (2017) An efficient hyperbolic shear deformation theory for bending, buckling and free vibration of FGM sandwich plates with various boundary conditions. Steel Compos Struct 25:693–704
124. Bellifa H, Bakora A, Tounsi A, Bousahla AA, Mahmoud S (2017) An efficient and simple four variable refined plate theory for buckling analysis of functionally graded plates. Steel Compos Struct 25:257–270
125. Fahsi A, Tounsi A, Hebali H, Chikh A, Adda Bedia E, Mahmoud S (2017) A four variable refined nth-order shear deformation theory for mechanical and thermal buckling analysis of functionally graded plates. Geomech Eng 13:385–410
126. Bousahla AA, Benyoucef S, Tounsi A, Mahmoud S (2016) On thermal stability of plates with functionally graded coefficient of thermal expansion. Struct Eng Mech 60:313–335
127. Boukhari A, Atmane HA, Tounsi A, Adda Bedia E, Mahmoud S (2016) An efficient shear deformation theory for wave propagation of functionally graded material plates. Struct Eng Mech 57:837–859
128. Beldjelili Y, Tounsi A, Mahmoud S (2016) Hygro-thermo-mechanical bending of S-FGM plates resting on variable elastic foundations using a four-variable trigonometric plate theory. Smart Struct Syst 18:755–786
129. Attia A, Tounsi A, Bedia E, Mahmoud S (2015) Free vibration analysis of functionally graded plates with temperature-dependent properties using various four variable refined plate theories. Steel Compos Struct 18:187–212
130. Wang Q (2002) On buckling of column structures with a pair of piezoelectric layers. Eng Struct 24:199–205
131. Reddy JN (2004) Mechanics of laminated composite plates and shells: theory and analysis. CRC Press, Boca Raton
132. Shu C (2012) Differential quadrature and its application in engineering. Springer, Berlin
133. Moayedi H, Darabi R, Ghabussi A, Habibi M, Foong LK (2020) Weld orientation effects on the formability of tailor welded thin steel sheets. Thin Walled Struct 149:106669
134. Ghazanfari A, Soleimani SS, Keshavarzzadeh M, Habibi M, Assempuor A, Hashemi R (2019) Prediction of FLD for sheet metal by considering through-thickness shear stresses. Mech Based Des Struct Mach. https://doi.org/10.1080/15397734.2019.1662310
135. Alipour M, Torabi MA, Sareban M, Lashini H, Sadeghi E, Fazaeli A et al (2019) Finite element and experimental method for analyzing the effects of martensite morphologies on the formability of DP steels. Mech Based Des Struct Mach. https://doi.org/10.1080/15397734.2019.1633343
136. Hosseini S, Habibi M, Assempour A (2018) Experimental and numerical determination of forming limit diagram of steel–copper two-layer sheet considering the interface between the layers. Modares Mech Eng 18:174–181
137. Habibi M, Hashemi R, Ghazanfari A, Naghdabadi R, Assempour A (2018) Forming limit diagrams by including the M–K model in finite element simulation considering the effect of bending. Proc Inst Mech Eng Part L J Mater Des Appl 232:625–636
138. Habibi M, Payganeh G (2018) Experimental and finite element investigation of titanium tubes hot gas forming and production of square cross-section specimens. Aerosp Mech J 14:89–99
139. Habibi M, Hashemi R, Tafti MF, Assempour A (2018) Experimental investigation of mechanical properties, formability and forming limit diagrams for tailor-welded blanks produced by friction stir welding. J Manuf Process 31:310–323

140. Habibi M, Ghazanfari A, Assempour A, Naghdabadi R, Hashemi R (2017) Determination of forming limit diagram using two modified finite element models. Mech Eng 48:141–144
141. Ghazanfari A, Assempour A, Habibi M, Hashemi R (2016) Investigation on the effective range of the through thickness shear stress on forming limit diagram using a modified Marciniak–Kuczynski model. Modares Mech Eng 16:137–143
142. Habibi M, Hashemi R, Sadeghi E, Fazaeli A, Ghazanfari A, Lashini H (2016) Enhancing the mechanical properties and formability of low carbon steel with dual-phase microstructures. J Mater Eng Perform 25:382–389
143. Fazaeli A, Habibi M, Ekrami A (2016) Experimental and finite element comparison of mechanical properties and formability of dual phase steel and ferrite–pearlite steel with the same chemical composition. Metall Eng 19(2):84–93
144. Shamloofard M, Assempour A (2019) Development of an inverse isogeometric methodology and its application in sheet metal forming process. Appl Math Model 73:266–284
145. Shamloofard M, Movahhedy MR (2015) Development of thermo-elastic tapered and spherical superelements. Appl Math Comput 265:380–399
146. Han J-B, Liew K (1999) Axisymmetric free vibration of thick annular plates. Int J Mech Sci 41:1089–1109

Publisher's Note Springer Nature remains neutral with regard to jurisdictional claims in published maps and institutional affiliations.